

A multi-dimensional, moment-accelerated deterministic particle method for time-dependent, multi-frequency thermal radiative transfer problems

Hans Hammer^{a,*}, HyeongKae Park^a, Luis Chacón^b

^a*Fluid Dynamics and Solid Mechanics (T-3)*

Los Alamos National Laboratory

Los Alamos, NM, 87545

^b*Applied Mathematics and Plasma Physics (T-5)*

Los Alamos National Laboratory

Los Alamos, NM, 87545

Abstract

Thermal Radiative Transfer (TRT) is the dominant energy transfer mechanism in high-energy density physics with applications in inertial confinement fusion and astrophysics. The stiff interactions between the material and radiation fields make TRT problems challenging to model. In this study, we propose a multi-dimensional extension of the deterministic particle (DP) method. The DP method combines aspects from both particle and deterministic methods. If the emission source is known *a priori*, and no physical scattering is present, the intensity of a particle can be integrated analytically. This introduces no statistical noise compared to Monte-Carlo methods, while maintaining the flexibility of particle methods. The method is closely related to the popular method of long characteristics. The combination of the DP-method with a discretely-consistent, nonlinear, gray low-order system enables an efficient solution algorithm for multi-frequency TRT problems. We demonstrate with numerical examples that the use of a linear-source approximation based on spatial moments improves the behavior of our method in the thick diffusion limit significantly.

Keywords: Thermal Radiative Transfer, HOLO algorithm, Deterministic particle method

*Corresponding author

Email addresses: hrhammer@lanl.gov (Hans Hammer), hkpark@lanl.gov (HyeongKae Park), chacon@lanl.gov (Luis Chacón)

1. Introduction

Many applications in astrophysics and plasma physics require the simulation of high-energy density phenomena. In these regimes, thermal X-ray radiation is the dominant mechanism of energy transfer. Thermal radiative transfer (TRT) is described by a system of stiff, nonlinear equations, and therefore difficult to model.

Two distinct methods are typically used, namely, the deterministic transport method and stochastic particle methods. Both methods have their advantages and disadvantages. A popular particle method is Implicit Monte Carlo (IMC)[8], which is based on a linearization of the reemission physics. The particle approach gives IMC flexibility for complicated geometries. The most common deterministic methods are the discrete ordinance or S_N method and the method of characteristics (MOC). Both are frequently used for neutron transport calculations in reactor physics. The advantage of S_N and MOC over IMC is that they do not show statistical noise, and they are able to obtain the asymptotic diffusion limit [15, 14, 13] in a relatively straightforward manner [1, 2].

A newly proposed deterministic particle (DP) method [21] combines these two approaches. If the emission source is known *a priori*, the intensity of a particle can be integrated analytically. In contrast to Monte-Carlo (MC) methods, our method does not feature any randomness (with the possible exception of particle initialization), and hence does not show stochastic noise, while maintaining the flexibility of particle methods. This method is similar to MOC in space and time proposed by Pandya and Adams [17]. However, our method is particle based, and therefore does not require fixed tracks.

When this DP solver is cast in a high-order, low-order (HOLO) algorithmic framework [4], a discretely-consistent, gray, nonlinear low-order (LO) system provides a well-informed emission source, acts as an interface with other physics in a multi-physics setting, and provides algorithmic acceleration [4]. Because of the presence of the consistent, nonlinear LO system, the emission source is known and the contribution from the absorption-emission physics can be analytically integrated along a particle's trajectory. This implicit treatment of the absorption-emission physics removes the explicit time step constraint, allowing us to choose the time step size based on accuracy, not stability.

The DP-HOLO method has been recently demonstrated in one dimension [21]. In this work we present the extension of the DP-HOLO method to multiple dimensions using a ray-tracing approach and a linear-source reconstruction scheme that preserves the diffusion limit. The flat-source approximation requires many cells in optically thick materials to model the changes in the temperature and the emission source sufficiently well. Introducing a linear reconstruction reduces the number of cells

necessary to obtain a good representation of the source. We use the method proposed by Ferrer and Rhodes III [6, 7] for MOC to obtain the linear representation of tallies. Adams et al. [2] showed that linear source representation on a triangular mesh, and bi-linear on orthogonal, rectangular meshes are required to obtain the thick diffusion limit. For general polygons, piecewise linear basis functions are required as shown by Pandya et al. [18], which again reduce to linear functions on triangles. Therefore, a linear-source reconstruction is also necessary to obtain the asymptotic diffusion limit [15, 14] with our method.

The remainder of the paper is structured as follows. We first introduce our method in Section 2, with the LO solver first followed by the HO solver. We then present numerical results to show the capabilities of this method in Section 3. We chose the Tophat [9] problem to demonstrate the effects of the linear source approximation and a planar Hohlraum problem [16, 3] to demonstrate the effects of different quadratures and random particle initialization. We compare our results to Capsaicin (which employs an S_N implementation) [24]. Finally, we show results for runtime and convergence studies of the algorithm before we conclude.

2. Method

Thermal radiative transfer without physical scattering can be described by the following system of equations

$$\frac{1}{c} \frac{\partial I}{\partial t} + \hat{\Omega} \cdot \nabla I + \sigma I = \sigma B \quad (1)$$

$$\rho c_v \frac{\partial T}{\partial t} = \int_0^\infty \int_{4\pi} (\sigma I - \sigma B) d\Omega d\nu \quad (2)$$

where $I(\mathbf{x}, \hat{\Omega}, \nu, t)$ is the specific radiation intensity at position \mathbf{x} traveling in along direction $\hat{\Omega}$ with the speed of light c and frequency ν at time t . Here, is the frequency integrated (gray) radiation energy density, $\sigma(\mathbf{x}, \nu, T)$ is the opacity at temperature T , ρ is the host material's density, and c_v is its specific heat capacity. The emission spectrum is defined by the Planck function

$$B(\nu, T) \equiv \frac{2h\nu^3}{c^2} \frac{1}{e^{h\nu/k_B T} - 1}, \quad (3)$$

where h denotes the Planck constant and k_B the Boltzmann constant.

Solving the TRT system is difficult due to the high dimensionality of the phase-space and the stiff, nonlinear coupling between the radiation field and the material temperature described by the absorption and emission physics.

The DP algorithm uses a high-order (HO), multi-frequency transport solve combined with a gray low-order solver (LO). For simplicity, we will describe the basic algorithm for the gray case and will extend it to the multi-frequency case afterwards. The gray TRT equation is

$$\frac{1}{c} \frac{\partial I}{\partial t} + \hat{\Omega} \cdot \nabla I + \sigma I = Q^{\text{LO}}(\mathbf{x}, t). \quad (4)$$

The DP method requires an *a priori* known emission source

$$Q^{\text{LO}}(\mathbf{x}, t) = \frac{\sigma a c T^4(\mathbf{x}, t)}{4\pi} \quad (5)$$

for the integration along the particle trajectory, where a is the radiation constant. Here, the LO superscript indicates that the source is evaluated from low-order quantities, obtained from a recently developed iterative, moment-based HOLO algorithm [19, 20, 4]. The LO system is defined by taking the first two angular moments of Eq. (4) together with the material temperature equation,

$$\frac{\partial E^{\text{LO}}}{\partial t} + \nabla \cdot \mathbf{F}^{\text{LO}} + \sigma c E^{\text{LO}} = \sigma a c T^4 + \mathcal{S}^{\text{HO}} \quad (6a)$$

$$\frac{1}{c} \frac{\partial \mathbf{F}^{\text{LO}}}{\partial t} + \frac{c}{3} \nabla E^{\text{LO}} + \sigma \mathbf{F}^{\text{LO}} = \gamma^{\text{HO}} c E^{\text{LO}} \quad (6b)$$

$$\rho c_v \frac{\partial T}{\partial t} + \sigma a c T^4 = \sigma c E^{\text{LO}}, \quad (6c)$$

where the HO superscript indicates that the quantity is evaluated using HO quantities,

$$E(\mathbf{x}, t) \equiv \frac{1}{c} \int_0^\infty \int_{4\pi} I d\Omega d\nu \quad (7)$$

is the frequency integrated (gray) radiation energy density, and

$$\mathbf{F}(\mathbf{x}, t) \equiv \int_0^\infty \int_{4\pi} \hat{\Omega} I d\Omega d\nu \quad (8)$$

is the gray radiative flux. We used the standard P_1 closure in Eq. (6b) instead of the more consistent Eddington tensor closure [11]. This introduces inconsistencies between the HO and LO descriptions, in addition to inconsistencies in the discretization. Adding the consistency term γ^{HO} to Eq. (6b) will correct for transport effects and the mismatch in truncation errors. While Eq. (6a) is exact in the continuum, we

advance that we will need to correct for mismatches between HO and LO temporal discretizations, and add the residual source term

$$\mathcal{S}^{\text{HO}} = \left. \frac{\partial E^{\text{HO}}}{\partial t} \right|_{\text{LO}} - \left. \frac{\partial E^{\text{HO}}}{\partial t} \right|_{\text{HO}}. \quad (9)$$

Here, the subscript LO indicates that we apply the LO discrete temporal derivative scheme, and similarly with the HO subscript. Both the LO and the HO methods conserve energy.

Both γ^{HO} and \mathcal{S}^{HO} are evaluated from the HO solution, and their specific form depends on the discretization used. Details will be discussed in the next section.

2.1. Low-order solver

The integral balance equation for Eq. (6a) obtained by integrating in time and cell volume is

$$\frac{\overline{E}_{i,n+\frac{1}{2}}^{\text{LO}} - \overline{E}_{i,n-\frac{1}{2}}^{\text{LO}}}{\Delta t_n} + \sum_{j \in i} \hat{\mathbf{n}}_{ij} \cdot \hat{\mathbf{n}}_j \frac{\overline{F}_{j,n}^{\text{LO}} A_j}{V_i} + \sigma_{i,n} c \overline{E}_{i,n}^{\text{LO}} - \sigma_{i,n} a c \overline{T_{i,n}^4} = 0 \quad (10)$$

where $\Delta t_n = t_{n+\frac{1}{2}} - t_{n-\frac{1}{2}}$ is the time step size for step n , V_i the cell volume, A_j the surface area, $\hat{\mathbf{n}}_j$ is the global unit normal of surface j and $\hat{\mathbf{n}}_{ij}$ is the unit normal of surface j pointing outwards from cell i . The sign of the product $\hat{\mathbf{n}}_j \cdot \hat{\mathbf{n}}_{ij}$ indicates if the flux is outgoing or incoming. The bar notation denotes a spatial average over a cell or surface. Note that we use half indices for end-of-time-step variables and integer indices for time averaged quantities. Therefore, we find

$$\overline{E}_{i,n+\frac{1}{2}} \equiv \frac{1}{cV_i} \int_{V_i} \int_{4\pi} I(\mathbf{x}, \hat{\Omega}, t_{n+\frac{1}{2}}) d\Omega dV \quad (11a)$$

$$\overline{E}_{i,n} \equiv \frac{1}{c\Delta t_n V_i} \int_{t_{n-\frac{1}{2}}}^{t_{n+\frac{1}{2}}} \int_{V_i} \int_{4\pi} I(\mathbf{x}, \hat{\Omega}, t) d\Omega dV dt \quad (11b)$$

$$\overline{F}_{j,n} \equiv \frac{1}{\Delta t_n A_j} \int_{t_{n-\frac{1}{2}}}^{t_{n+\frac{1}{2}}} \int_{A_j} \int_{4\pi} \hat{\mathbf{n}}_j \cdot \hat{\Omega} I(\mathbf{x}, \hat{\Omega}, t) d\Omega dA dt \quad (11c)$$

$$\overline{T_{i,n}^4} \equiv \frac{1}{\Delta t_n V_i} \int_{t_{n-\frac{1}{2}}}^{t_{n+\frac{1}{2}}} \int_{V_i} T^4(\mathbf{x}, t) dV dt \quad (11d)$$

The time-discrete LO equation cannot update simultaneously quantities defined at n and $n + \frac{1}{2}$, and therefore we replace end-of-time-step quantities with time step average quantities by adding a residual source term:

$$\frac{\overline{E}_{i,n}^{\text{LO}} - \overline{E}_{i,n-1}^{\text{LO}}}{\Delta t_n} + \sum_{j \in i} \hat{\mathbf{n}}_{ij} \cdot \hat{\mathbf{n}}_j \frac{\overline{F}_{j,n}^{\text{LO}} A_j}{V_i} + \sigma_{i,n} c \overline{E}_{i,n}^{\text{LO}} - \sigma_{i,n} a c \overline{T_{i,n}^4} = \mathcal{S}_{i,n}^{\text{HO}}, \quad (12)$$

where the residual source is defined as:

$$\mathcal{S}_{i,n}^{\text{HO}} \equiv \frac{\bar{E}_{i,n}^{\text{HO}} - \bar{E}_{i,n-1}^{\text{HO}}}{\Delta t_n} - \frac{\bar{E}_{i,n+\frac{1}{2}}^{\text{HO}} - \bar{E}_{i,n-\frac{1}{2}}^{\text{HO}}}{\Delta t_n}. \quad (13)$$

The discrete equation for the flux $\bar{F}_{j,n}$ across surface j using the method proposed by Park et al. [21] can be written as

$$\frac{1}{c} \frac{\bar{F}_{j,n}^{\text{LO}} - \bar{F}_{j,n-1}^{\text{LO}}}{\Delta t_n} + \frac{c}{3} \frac{\bar{E}_{j+\frac{1}{2},n}^{\text{LO}} - \bar{E}_{j-\frac{1}{2},n}^{\text{LO}}}{\Delta x_j} + \sigma_{j,n} \bar{F}_{j,n}^{\text{LO}} = \gamma_{j,n}^{+\text{HO}} c \bar{E}_{j+\frac{1}{2},n}^{\text{LO}} - \gamma_{j,n}^{-\text{HO}} c \bar{E}_{j-\frac{1}{2},n}^{\text{LO}}. \quad (14)$$

where the indices $j \pm \frac{1}{2}$ denote the cells adjacent to surface j , Δx_j is the characteristic length between these cells, and $\sigma_{j,n}$ is a weighted opacity at the surface. The consistency terms are given by [19]

$$\gamma_{j,n}^{+\text{HO}} = \frac{1}{c \bar{E}_{j+\frac{1}{2},n}^{\text{HO}}} \left(\frac{1}{c} \frac{f_{j,n}^{+\text{HO}} - f_{j,n-1}^{+\text{HO}}}{\Delta t_n} + \frac{c}{6} \frac{\bar{E}_{j+\frac{1}{2},n}^{\text{HO}} - \bar{E}_{j-\frac{1}{2},n}^{\text{HO}}}{\Delta x_j} + \sigma_{j,n} f_{j,n}^{+\text{HO}} \right) \quad (15a)$$

$$\gamma_{j,n}^{-\text{HO}} = \frac{1}{c \bar{E}_{j-\frac{1}{2},n}^{\text{HO}}} \left(\frac{1}{c} \frac{f_{j,n}^{-\text{HO}} - f_{j,n-1}^{-\text{HO}}}{\Delta t_n} - \frac{c}{6} \frac{\bar{E}_{j+\frac{1}{2},n}^{\text{HO}} - \bar{E}_{j-\frac{1}{2},n}^{\text{HO}}}{\Delta x_j} + \sigma_{j,n} f_{j,n}^{-\text{HO}} \right) \quad (15b)$$

where the partial fluxes are defined from the HO solution with respect to the global surface normal $\hat{\mathbf{n}}_j$ as

$$f_{j,n}^+ \equiv \frac{1}{\Delta t_n} \int_{t_{n-\frac{1}{2}}}^{t_{n+\frac{1}{2}}} \int_{A_j} \int_{\hat{\Omega} \cdot \hat{\mathbf{n}}_j > 0} \hat{\mathbf{n}}_j \cdot \hat{\Omega} I(\mathbf{x}, \hat{\Omega}, t) d\Omega dA dt \quad (16a)$$

$$f_{j,n}^- \equiv -\frac{1}{\Delta t_n} \int_{t_{n-\frac{1}{2}}}^{t_{n+\frac{1}{2}}} \int_{A_j} \int_{\hat{\Omega} \cdot \hat{\mathbf{n}}_j < 0} \hat{\mathbf{n}}_j \cdot \hat{\Omega} I(\mathbf{x}, \hat{\Omega}, t) d\Omega dA dt. \quad (16b)$$

Finally, the flux across the boundary surface j is

$$\bar{F}_{j,n} = f_{j,n}^+ - f_{j,n}^- = (1 - \alpha_j) f_{j,n}^+ - f_{j,n}'^- \quad (17)$$

where we assume the normal points outwards, and $\alpha_j \in [0,1]$ is the reflection or albedo factor. It allows the user to define boundaries as vacuum, partially or fully reflecting. The incoming boundary flux without reflection is

$$f_{j,n}'^- = f_{j,n}^- - \alpha_j f_{j,n}^+ = \frac{acT_{\text{BC},j}^4}{4}. \quad (18)$$

Defining the boundary factors

$$\kappa_{j,n}^{+\text{HO}} \equiv \frac{f_{j,n}^{+\text{HO}}}{c\bar{E}_{j-\frac{1}{2},n}^{\text{HO}}} \quad (19\text{a})$$

$$\kappa_{j,n}^{-\text{HO}} \equiv \begin{cases} 0 & T_{\text{BC},j} = 0 \\ \frac{f_{j,n}^{-\text{HO}} - \alpha_j f_{j,n}^{+\text{HO}}}{acT_{\text{BC},j}^4} & T_{\text{BC},j} > 0 \end{cases} \quad (19\text{b})$$

gives the LO boundary condition

$$\bar{F}_{j,n}^{\text{LO}} = (1 - \alpha_j) \kappa_{j,n}^{+\text{HO}} c\bar{E}_{i-\frac{1}{2},n}^{\text{LO}} - \kappa_{j,n}^{-\text{HO}} acT_{\text{BC},j}^4. \quad (20)$$

In these equations, \mathcal{S}^{HO} , $\gamma_{j,n}^{\pm\text{HO}}$ and $\kappa_{j,n}^{\pm\text{HO}}$ are evaluated from the HO system using Eqs. (11) and (16). This gives discrete consistency between the LO and HO system. The LO-system is solved using a Newton-Krylov method with non-linear elimination [19]. The details are given in Appendix A.1.

Finally, the temperature equation, Eq. (6c), is discretized as

$$\rho c_v \frac{\bar{T}_{i,n}^{\text{LO}} - \bar{T}_{i,n-1}^{\text{LO}}}{\Delta t_n} + \sigma_{i,n} ac\bar{T}_{i,n}^4 - \sigma_{i,n} c\bar{E}_{i,n}^{\text{LO}} = 0. \quad (21)$$

2.2. High-order solver

The high-order solver is a particle-based ray-tracing algorithm. In particle-based methods (e.g. Monte Carlo) the angular intensity I is represented as a collection of P particles with their specific intensity I_p^{HO} as

$$I^{\text{HO}}(\mathbf{x}, \hat{\Omega}, t) = \sum_{p=1}^P w_p I_p^{\text{HO}}(t) \delta(\mathbf{x} - \mathbf{x}_p(t)) \delta(\|\hat{\Omega} - \hat{\Omega}_p(t)\|) \quad (22)$$

where $\mathbf{x}_p(t)$, $\hat{\Omega}_p(t)$ are the spatial position and direction of particle p at time t . The particle phase-space volume w_p is the analog to the track width of MOC methods, an integral weight factor. Details of its calculation are given later. The evolution equation of the particle intensity can be found by multiplying Eq. (4) by $\delta(\mathbf{x} - \mathbf{x}_p(t)) \delta(\|\hat{\Omega} - \hat{\Omega}_p(t)\|)$ and integrating over the phase-space to obtain

$$\frac{1}{c} \frac{dI_p^{\text{HO}}}{dt} + \sigma I_p^{\text{HO}} = Q^{\text{LO}}(x_p, t) \quad (23)$$

where $Q^{\text{HO}}(x, t)$ is the *a priori* known emission source Eq. (5). The formal solution for I_p^{HO} along the characteristic for particle p in cell i at time step n is

$$I_{p,i,n}^{\text{HO}}(t) = I_{p,i,n}^{\text{HO}}(t_0) e^{-\int_{t_0}^t \sigma c dt'} + \int_{t_0}^t e^{-\int_{t'}^t \sigma_{i,n} c dt''} Q_{i,n}^{\text{LO}}(\mathbf{x}_p(t'), t') c dt'. \quad (24)$$

This equation, and its first spatial moment, can be integrated analytically when one considers a linear emission source (as will be the case here), and that particle trajectories are straight. We consider the particle initialization and trajectory computation next.

2.2.1. Particle initialization

The particles are initialized on a per-cell basis. In each cell i , a number of points are selected as starting points for the particles. The points are found by increasingly refining the cell up to a specified level. Each triangle or rectangle cell is divided into four subcells, until the level of requested refinement is reached. After the cell is refined, the particles are initialized at the center point of each subcell ζ with the volume V_ζ . The particles at each point are launched in the direction of a given angular quadrature with corresponding weights $\{\hat{\Omega}_m, \omega_m\}_{m=1}^M$. This quadrature can be deterministic or random. The particle phase-space factor is

$$w_p \equiv V_\zeta \omega_m \quad (25)$$

and must satisfy

$$\sum_{p \in i} w_p = 4\pi V_i. \quad (26)$$

In this work, we assume initial conditions that are isotropic in angle and Planckian in frequency. Therefore the initial radiation energy density can be described with

$$\bar{E}_{i,\frac{1}{2}} = aT_{i,\frac{1}{2}}^4 \quad (27)$$

where $T_{i,\frac{1}{2}}$ is the initial temperature at $t = 0$. Using Eq. (22) and the definition of the radiation energy density, Eq. (7), we find

$$I_{p,i,\frac{1}{2}}^{\text{HO}} = \frac{acT_{i,\frac{1}{2}}^4}{4\pi}. \quad (28)$$

2.2.2. Particle trajectory

Since no accelerating forces affect the particles, their trajectory can be simply expressed as a straight ray

$$\mathbf{x}_p(t) = \mathbf{x}_{0,p} + ct\hat{\Omega}_p \quad (29)$$

from $\mathbf{x}_{0,p} = \mathbf{x}_p(t_0)$ in direction $\hat{\Omega}_p$. In curvilinear geometry, local orthogonal coordinates can be used [22]. The distance a particle travels within a timestep is $s_p = c\Delta t$. The particle movement is subdivided by intersections with cell surfaces. Each subdivision produces a straight track, contained within one cell with constant material properties. After each track, either the cell changes, the particle is reflected at a boundary or the end of the time step is reached. The calculation of intersections is a common problem in computational geometry or graphics applications and many efficient algorithms for all types of surfaces can be found in literature [10]. We limit our mesh to cells that are strictly convex with planar surfaces. In this case, the intersection between a ray originating from within the cell and the surface of the cell is the shortest positive distance to all of the surfaces. This approach allows us to avoid costly vertex comparisons to determine which surface the particle goes through.

An infinite, planar surface in three dimensions is fully described by the implicit definition

$$\hat{\mathbf{n}} \cdot \mathbf{x} - b = 0 \quad (30)$$

where $\hat{\mathbf{n}} \in \mathbb{R}^3$ is the normal of the surface and $b \in \mathbb{R}$ is the offset. With Eq. (29) the distance the particle has to travel to cross surface j from its origin $\mathbf{x}_{0,p,i,n}$ in cell i at time step n can be found as

$$s_{j,p,i,n} = \frac{b_j - \hat{\mathbf{n}}_j \cdot \mathbf{x}_{0,p,i,n}}{\hat{\mathbf{n}}_j \cdot \hat{\Omega}_p}. \quad (31)$$

The surfaces are extended to infinity beyond the limits of the cell. Therefore, there is an intersection with the ray, if

$$\hat{\mathbf{n}}_j \cdot \hat{\Omega}_p \neq 0, \quad (32)$$

otherwise the surface and the ray are parallel. The relevant intersection of the ray is then the intersection with the smallest positive distance

$$s_{p,i,n} = \min_j s_{j,p,i,n} \quad \text{for } s_{j,p,i,n} > 0. \quad (33)$$

Special care is necessary if the particle hits a corner as detailed in Appendix A.2. The time it takes the particle to reach the surface is

$$\Delta t_{s,i} = \frac{s_{p,i,n}}{c} \quad (34)$$

and it must be smaller than the remaining time Δt_p in the time step. Otherwise the particle cannot reach the surface within the time step. In this case, the particle is simply moved to its end of time step position

$$\mathbf{x}_p = \mathbf{x}_{0,p} + c\Delta t_p \hat{\Omega}. \quad (35)$$

The remaining time of the particle is updated by

$$\Delta t'_p = \Delta t_p - \Delta t_{s,i}. \quad (36)$$

If a particle crosses a surface that is part of the boundary, it is always reflected back into the domain. Therefore, the number of particles remain constant throughout the calculation. The new direction is found by the reflection law

$$\hat{\Omega}'_p = \hat{\Omega}_p - 2(\hat{\mathbf{n}}_j \cdot \hat{\Omega}_p) \cdot \hat{\mathbf{n}}_j \quad (37)$$

and the intensity is

$$I'_{p,j,n}{}^{\text{HO}} = \alpha_j I_{p,j,n}{}^{\text{HO}} + \frac{acT_{\text{BC},j}^4}{4\pi} \quad (38)$$

where α_j is the reflection factor. This provides both vacuum ($\alpha = 0$) and reflective ($\alpha = 1$) conditions, and in between. For vacuum boundaries with no influx, the intensity is set to $I'_{p,j,n}{}^{\text{HO}} = 0$, but it evolves according to Eq. (24).

2.2.3. Linear source approximation and tallying

To solve the characteristic equation, Eq. (24), effectively, we must be able to evaluate the source term $Q^{LO}(\mathbf{x}_p(t), t)$ given LO quantities. A key consideration for the source evaluation is the need to capture the asymptotic diffusion limit (a critical numerical property [15, 14, 13]), for which a linear (or higher order) representation of the relevant quantities E and T is needed [5, 6, 7, 25]. Here, we consider a linear source reconstruction. However, linear descriptions are not without issues. They increase the computational cost per cell and, depending on the slope, may violate positivity (see Appendix A.3 for our treatment to enforce positivity of the source). This may occur for cells with low temperatures and steep gradients, e.g., at boundary layers and at thermal fronts. Finally, not all linear source reconstructions capture correctly the asymptotic diffusion limit. In what follows, following Ferrer and Rhodes III [6, 7], we first outline a general linear-reconstruction procedure for an arbitrary function that will yield a method able to capture the asymptotic diffusion limit. Later, we use this reconstruction for the emission source in the HO solver, and derive the corresponding moment tallies needed.

Linear reconstruction procedure. Let $\phi_{i,n}(\mathbf{x})$ be a quantity evaluated by scoring of particles in cell i and timestep n , which can be an arbitrary function in $\mathbf{x} \in V_i$. We seek its linear representation $\psi_{i,n}(\mathbf{x})$ within the same cell i . For simplicity, let $\phi_{i,n}$ be angle-independent, to focus on the spatial aspect. Its zeroth spatial moment is

$$\begin{aligned}\bar{\phi}_{i,n} &= \frac{1}{V_i} \int_{V_i} \phi_{i,n}(\mathbf{x}) dV \\ &= \frac{1}{4\pi V_i} \sum_{p=1}^{P_i} w_p \int_0^{s_{p,i,n}} \phi_{i,n}(\mathbf{x}(s')) ds',\end{aligned}\quad (39)$$

and its first spatial moment is

$$\begin{aligned}\tilde{\phi}_{i,n} &= \frac{1}{V_i} \int_{V_i} \mathbf{x} \phi_{i,n}(\mathbf{x}) dV \\ &= \frac{1}{4\pi V_i} \sum_{p=1}^{P_i} w_p \int_0^{s_{p,i,n}} \mathbf{x}(s') \phi_{i,n}(\mathbf{x}(s')) ds',\end{aligned}\quad (40)$$

where $s_{p,i,n}$ is the track of particle p in cell i at time step n , w_p denotes the particle's phase-space volume, and P_i is the number of particles in cell i .

We consider the following ansatz for the linear representation of $\phi_{i,n}$ in cell i

$$\psi_{i,n}(\mathbf{x}) = \bar{\psi}_{i,n} + \tilde{\psi}_{i,n} \cdot (\mathbf{x} - \mathbf{x}_{C,i}) \quad (41)$$

where $\bar{\psi}_{i,n}$ is the constant part and the vector $\tilde{\psi}_{i,n}$ is its gradient. We will adopt this notation also for other linear quantities throughout this paper. In Eq. (41),

$$\mathbf{x}_{C,i} = \frac{1}{V_i} \int_{V_i} \mathbf{x} dV. \quad (42)$$

is the center of mass of the cell i . The following property follows:

$$\frac{1}{V_i} \int_{V_i} \psi_{i,n}(\mathbf{x}) dV = \bar{\psi}_{i,n} \quad (43)$$

Also, by definition:

$$\frac{1}{V_i} \int_{V_i} (\mathbf{x} - \mathbf{x}_{C,i}) dV = 0. \quad (44)$$

Since the spatial moments of the linear representation must equal the scored spatial moments, the zeroth moment must satisfy:

$$\frac{1}{V_i} \int_{V_i} \psi_{i,n}(\mathbf{x}) dV = \bar{\phi}_{i,n} \quad (45)$$

and hence with Eq. (43)

$$\bar{\psi}_{i,n} = \bar{\phi}_{i,n}. \quad (46)$$

To approximate the gradient, we compute the first spatial moment as:

$$\frac{1}{V_i} \int_{V_i} (\mathbf{x} - \mathbf{x}_{C,i}) \psi_{i,n}(\mathbf{x}) dV = \frac{1}{V_i} \int_{V_i} (\mathbf{x} - \mathbf{x}_{C,i}) \phi_{i,n}(\mathbf{x}) dV, \quad (47)$$

which with Eqs. (39) to (41) gives the equation system

$$\tilde{\psi}_{i,n} \frac{1}{V_i} \int_{V_i} (\mathbf{x} - \mathbf{x}_{C,i}) \otimes (\mathbf{x} - \mathbf{x}_{C,i}) dV = \tilde{\phi}_{i,n} - \mathbf{x}_{C,i} \bar{\phi}_{i,n} \quad (48)$$

where \otimes denotes the tensor product. Written algebraically, the solution is

$$\tilde{\psi}_{i,n} = \mathbf{M}_i^{-1} \left(\tilde{\phi}_{i,n} - \bar{\phi}_{i,n} \mathbf{x}_{C,i} \right) \quad (49)$$

where the matrix

$$\mathbf{M}_i = \frac{1}{V_i} \int_{V_i} (\mathbf{x} - \mathbf{x}_{C,i}) \otimes (\mathbf{x} - \mathbf{x}_{C,i}) dV \quad (50)$$

only contains geometric information [23], and can be precomputed for each cell.

Linear reconstruction of the emission source. Using the linear approximation, Eq. (41), the source in cell i for time step n has the form

$$Q_{i,n}^{\text{LO}}(\mathbf{x}) = \bar{Q}_{i,n}^{\text{LO}} + \tilde{\mathbf{Q}}_{i,n}^{\text{LO}} \cdot (\mathbf{x} - \mathbf{x}_{C,i}). \quad (51)$$

where $\bar{Q}_{i,n}^{\text{LO}}$ is the average and $\tilde{\mathbf{Q}}_{i,n}^{\text{LO}}$ the source gradient. We begin by introducing the auxiliary variable

$$\Theta_{i,n}(\mathbf{x}) = T_{i,n}^4(\mathbf{x}) \quad (52)$$

so that the source term can be written as

$$\begin{aligned} Q_{i,n}^{\text{LO}}(\mathbf{x}) &= \sigma_{i,n} ac \Theta_{i,n}(\mathbf{x}) \\ &= \sigma_{i,n} ac \left(\bar{\Theta}_{i,n} + \tilde{\Theta}_{i,n} \cdot (\mathbf{x} - \mathbf{x}_{C,i}) \right). \end{aligned} \quad (53)$$

The temperature is linearized by expanding $\Theta_{i,n}(\mathbf{x})$ using a Taylor series

$$\begin{aligned} T_{i,n}(\mathbf{x}) &= \sqrt[4]{\bar{\Theta}_{i,n}} + \frac{1}{4} \bar{\Theta}_{i,n}^{-\frac{3}{4}} \tilde{\Theta}_{i,n} \cdot (\mathbf{x} - \mathbf{x}_{C,i}) \\ &= \bar{T}_{i,n} + \tilde{\mathbf{T}}_{i,n} \cdot (\mathbf{x} - \mathbf{x}_{C,i}). \end{aligned} \quad (54)$$

The cell-average temperature, $\bar{T}_{i,n}$, is updated according to the evolution equation obtained by integrating Eq. (6c) over time step n and cell i [and using Eq. (43)]:

$$\frac{\rho c_v}{\Delta t_n} (\bar{T}_{i,n} - \bar{T}_{i,n-1}) + \sigma_{i,n} ac \bar{\Theta}_{i,n} - \sigma_{i,n} c \bar{E}_{i,n}^{\text{LO}} = 0 \quad (55)$$

For the temperature gradient, $\tilde{\mathbf{T}}_{i,n}$, we use the first spatial moment of Eq. (6c),

$$\frac{1}{V_i \Delta t_n} \int_{\Delta t_n} \int_{V_i} (\mathbf{x} - \mathbf{x}_{C,i}) \left[\rho c_v \frac{\partial T_{i,n}(\mathbf{x})}{\partial t} + \sigma ac \Theta_{i,n}(\mathbf{x}) - \sigma_{i,n} c E_{i,n}^{\text{LO}}(\mathbf{x}) \right] dV dt = 0 \quad (56)$$

to obtain

$$\frac{1}{V_i} \int_{V_i} (\mathbf{x} - \mathbf{x}_{C,i}) \otimes (\mathbf{x} - \mathbf{x}_{C,i}) dV \cdot \left[\frac{\rho c_v}{\Delta t_n} (\tilde{\mathbf{T}}_{i,n} - \tilde{\mathbf{T}}_{i,n-1}) + \sigma_{i,n} ac \tilde{\Theta}_{i,n} - \sigma_{i,n} c \tilde{E}_{i,n}^{\text{LO}} \right] = 0. \quad (57)$$

Using Eq. (54), we can solve this equation for the gradient of $\Theta_{i,n}$ as a function of the gradient of $E_{i,n}^{\text{LO}}$:

$$\tilde{\Theta}_{i,n} = \frac{\frac{\rho c_v}{4\Delta t_n} \bar{\Theta}_{i,n-1}^{-\frac{3}{4}} \tilde{\Theta}_{i,n-1} + \sigma_{i,n} c \tilde{E}_{i,n}^{\text{LO}}}{\frac{\rho c_v}{4\Delta t_n} \bar{\Theta}_{i,n}^{-\frac{3}{4}} + \sigma_{i,n} ac}. \quad (58)$$

For simplicity, the LO gradient of $E_{i,n}$ is found in this study by scaling its HO gradient as:

$$\tilde{\mathbf{E}}_{i,n}^{\text{LO}} = \tilde{\mathbf{E}}_{i,n}^{\text{HO}} \frac{\bar{E}_{i,n}^{\text{LO}}}{\bar{E}_{i,n}^{\text{HO}}} \quad (59)$$

A better choice would be to discretize the LO system with Discontinuous Galerkin (DG), but we leave this for future work. Thus, all that remains is to tally the HO average and gradient components of $E_{i,n}$. We explain next how this is done.

Tallying of HO moments. Combining the linearized emission source, Eq. (54), with the particle equation of motion, Eq. (29), yields the emission source for a specific particle p :

$$Q_{p,i,n}^{\text{LO}}(s) = \bar{Q}_{i,n}^{\text{LO}} + \tilde{Q}_{i,n}^{\text{LO}} \cdot (\mathbf{x}_{0,p,i,n} - \mathbf{x}_{C,i} + s \hat{\Omega}_p) = \bar{q}_{p,i,n}^{\text{LO}} + s \tilde{q}_{p,i,n}^{\text{LO}},$$

which is a linear function of the orbit distance, s . Within a cell, the material properties and opacities are assumed to be constant and given by

$$\sigma_{i,n} = \sigma(\mathbf{x}_{C,i}, \bar{T}_{i,n-1}). \quad (60)$$

We can now analytically solve the integral in Eq. (24) and obtain the intensity function

$$I_{p,i,n}^{\text{HO}}(s) = I_{p,i,n}^{\text{HO}}(0) e^{-\sigma_{i,n}s} + \left(\bar{q}_{p,i,n}^{\text{LO}} - \frac{\tilde{q}_{p,i,n}^{\text{LO}}}{\sigma_{i,n}} \right) \frac{G(\sigma_{i,n}s)}{\sigma_{i,n}} + s \frac{\tilde{q}_{p,i,n}^{\text{LO}}}{\sigma_{i,n}}, \quad (61)$$

with $G(\tau) = (1 - e^{-\tau})$. Note that, with the known emission source, the particle intensity asymptotes to the equilibrium solution (instead of zero) in optically thick regimes, which results in much improved behavior compared to MC.

With the intensity analytically known, we can analytically tally the contribution of particle p in cell i to the average and gradient of the radiation energy density. The average radiation energy density per particle is found as:

$$\begin{aligned} \overline{\delta E}_{p,i,n}^{\text{HO}} &= \int_0^{s_{p,i,n}} I_{p,i,n}^{\text{HO}}(s') ds' \\ &= I_{p,i,n}^{\text{HO}}(0) \frac{G(\sigma_{i,n}s_{p,i,n})}{\sigma_{i,n}} + \frac{1}{\sigma_{i,n}} \left(\bar{q}_{p,i,n}^{\text{LO}} - \frac{\tilde{q}_{p,i,n}^{\text{LO}}}{\sigma_{i,n}} \right) \\ &\quad \cdot \left(s_{p,i,n} - \frac{G(\sigma_{i,n}s_{p,i,n})}{\sigma_{i,n}} \right) + \frac{s_{p,i,n}^2}{2\sigma_{i,n}} \tilde{q}_{p,i,n}^{\text{LO}}. \end{aligned} \quad (62)$$

The average radiation energy density in cell i is found as the sum of all particle contributions

$$\bar{E}_{i,n}^{\text{HO}} = \frac{1}{V_i c^2 \Delta t_n} \sum_{p=1}^{P_i} w_p \overline{\delta E}_{p,i,n}^{\text{HO}}. \quad (63)$$

Per Eq. (40), the gradient of the radiation energy density is calculated from the first spatial moment of the intensity function, with a single particle contribution given by:

$$\begin{aligned} \widetilde{\delta \mathbf{E}}_{p,i,n}^{\text{HO}} &= \int_0^{s_{p,i,n}} \mathbf{x}(s') I_{p,i,n}^{\text{HO}}(s') ds' \\ &= \mathbf{x}_{0,p,i,n} \int_0^{s_{p,i,n}} I_{p,i,n}^{\text{HO}}(s') ds' + \hat{\Omega}_p \int_0^{s_{p,i,n}} s' I_{p,i,n}^{\text{HO}}(s') ds', \end{aligned} \quad (64)$$

where we used Eq. (29) for the particle orbit. The first integral in Eq. (64) is $\overline{\delta E}_{p,i,n}$, Eq. (62), and the second integral gives

$$\begin{aligned} \int_0^{s_{p,i,n}} s' I_{p,i,n}^{\text{HO}}(s') ds' &= \left(\frac{G(\sigma_{i,n}s_{p,i,n})}{\sigma_{i,n}^2} - \frac{s_{p,i,n}}{\sigma_{i,n}} e^{-\sigma_{i,n}s_{p,i,n}} \right) I_{p,i,n}^{\text{HO}}(0) + \frac{s_{p,i,n}^3}{3\sigma_{i,n}} \tilde{q}_{p,i,n}^{\text{LO}} \\ &\quad + \left(\bar{q}_{p,i,n}^{\text{LO}} - \frac{\tilde{q}_{p,i,n}^{\text{LO}}}{\sigma_{i,n}} \right) \left(\frac{s_{p,i,n}^2}{2\sigma_{i,n}} + \frac{s_{p,i,n}}{\sigma_{i,n}^2} e^{-\sigma_{i,n}s_{p,i,n}} - \frac{G(\sigma_{i,n}s_{p,i,n})}{\sigma_{i,n}^3} \right). \end{aligned} \quad (65)$$

Projecting the gradient according to Eq. (49), the linear reconstruction of the gradient of the radiation energy density reads:

$$\widetilde{\mathbf{E}}_{i,n}^{\text{HO}} = \mathbf{M}^{-1} \left[\frac{1}{V_i c^2 \Delta t_n} \sum_{p=1}^{P_i} w_p \widetilde{\delta \mathbf{E}}_{p,i,n}^{\text{HO}} - \mathbf{x}_{C,i} \overline{E}_{i,n}^{\text{HO}} \right]. \quad (66)$$

It is useful to point out that, in voids ($\sigma_{i,n} = 0$) Eqs. (61), (62) and (64) simplify to

$$I_{p,i,n}^{\text{HO}}(s) = I_{p,i,n}^{\text{HO}}(0), \quad (67a)$$

$$\overline{\delta E}_{p,i,n}^{\text{HO}} = s I_{p,i,n}^{\text{HO}}(0), \quad (67b)$$

$$\widetilde{\delta \mathbf{E}}_{p,i,n}^{\text{HO}} = \frac{s^2}{2} I_{p,i,n}^{\text{HO}}(0) \hat{\Omega}_p, \quad (67c)$$

while Eqs. (63) and (66) remain the same.

Other required tallies include the end-of-time-step radiation energy density, which is the census of particles within a cell:

$$\overline{E}_{i,n+\frac{1}{2}}^{\text{HO}} = \frac{1}{c V_i} \sum_{p=1}^{P_i} w_p I_{p,i,n+\frac{1}{2}}^{\text{HO}}, \quad (68)$$

and the partial fluxes across surface j , which are the sum of intensities of all particles crossing it:

$$f_{j,n}^{+\text{HO}} = \frac{1}{A_j c \Delta t_n} \sum_{p=1}^{P_j} w_p I_{p,j,n}^{\text{HO}} \quad \text{for } \hat{\Omega}_p \cdot \hat{\mathbf{n}}_j > 0, \quad (69a)$$

$$f_{j,n}^{-\text{HO}} = \frac{1}{A_j c \Delta t_n} \sum_{p=1}^{P_j} w_p I_{p,j,n}^{\text{HO}} \quad \text{for } \hat{\Omega}_p \cdot \hat{\mathbf{n}}_j < 0. \quad (69b)$$

2.3. Multi-frequency extension

For frequency-dependent problems, we employ the standard multi-frequency discretization. The specific angular intensity I_g for group g is defined as

$$I_g^{\text{HO}}(\mathbf{x}, \hat{\Omega}, t) = \int_{\nu_{g-\frac{1}{2}}}^{\nu_{g+\frac{1}{2}}} I(\mathbf{x}, \hat{\Omega}, \nu, t) d\nu. \quad (70)$$

This leads to the multi-group TRT equation

$$\frac{1}{c} \frac{\partial I_g^{\text{HO}}}{\partial t} + \hat{\Omega} \cdot \nabla I_g^{\text{HO}} + \sigma_g I_g^{\text{HO}} = \frac{\sigma_g b_g a c T^4}{4\pi}, \quad (71)$$

where

$$b_g(T) = \frac{\int_{\nu_{g-\frac{1}{2}}}^{\nu_{g+\frac{1}{2}}} B(\nu, T) d\nu}{\int_0^\infty B(\nu, T) d\nu} = \frac{\int_{\nu_{g-\frac{1}{2}}}^{\nu_{g+\frac{1}{2}}} B(\nu, T) d\nu}{\frac{1}{4\pi} acT^4} \quad (72)$$

is the Planck Spectrum factor. The characteristic solution along a particle trajectory, Eq. (24), can be written as

$$I_{g,p}^{\text{HO}}(t) = I_{g,p}^{\text{HO}}(t_0) e^{-\int_{t_0}^t \sigma_g c dt'} + \int_{t_0}^t e^{-\int_{t'}^t \sigma_g c dt''} Q_g^{\text{LO}}(\mathbf{x}_p(t'), t') c dt' \quad (73)$$

with

$$Q_g^{\text{LO}}(\mathbf{x}, t') = \frac{b_g acT^4(\mathbf{x}, t')}{4\pi}. \quad (74)$$

Using the same procedure as in Section 2.2, the group-wise quantities $I_{p,i,n}^{\text{HO}}(s)$, $\overline{\delta E}_{g,p,i,n}^{\text{HO}}$, $\widetilde{\delta \mathbf{E}}_{g,p,i,n}^{\text{HO}}$ are calculated the same as the gray counterparts in Eqs. (61), (62) and (64), respectively, using $I_{g,p,i,n}^{\text{HO}}$, $\bar{q}_{g,p,i,n}^{\text{LO}}$, $\tilde{q}_{g,p,i,n}^{\text{LO}}$ and $\sigma_{g,i,n}$. The tallied quantities then become

$$\overline{E}_{i,n}^{\text{HO}} = \frac{1}{V_i c^2 \Delta t_n} \sum_{p=1}^{P_i} w_p \sum_{g=1}^G \overline{\delta E}_{g,p,i,n}^{\text{HO}} \quad (75)$$

$$\widetilde{\mathbf{E}}_{i,n}^{\text{HO}} = \mathbf{M}^{-1} \left[\frac{1}{V_i c^2 \Delta t_n} \sum_{p=1}^{P_i} w_p \sum_{g=1}^G \widetilde{\delta \mathbf{E}}_{g,p,i,n}^{\text{HO}} - \mathbf{x}_{C,i} \overline{E}_{i,n}^{\text{HO}} \right] \quad (76)$$

$$\overline{E}_{i,n+\frac{1}{2}}^{\text{HO}} = \frac{1}{c V_i} \sum_{p=1}^{P_i} w_p \sum_{g=1}^G I_{g,p,i,n+\frac{1}{2}}^{\text{HO}} \quad (77)$$

$$f_{j,n}^{\pm \text{HO}} = \frac{1}{A_j c \Delta t_n} \sum_{p=1}^{P_j} w_p \sum_{g=1}^G I_{g,p,j,n}^{\text{HO}} \quad \text{for } \hat{\Omega}_p \cdot \hat{\mathbf{n}}_j \gtrless 0 \quad (78)$$

with the only difference being the summation over the groups.

The LO-system remains gray in the multi-frequency case. However, the opacities must be changed to weighted opacities [26]. The LO-system becomes

$$\frac{\partial E^{\text{LO}}}{\partial t} + \nabla \cdot \mathbf{F}^{\text{LO}} + \sigma_{\text{E}}^{\text{HO}} c E^{\text{LO}} - \sigma_{\text{P}} acT^4 = \mathcal{S}^{\text{HO}}, \quad (79a)$$

$$\frac{1}{c} \frac{\partial \mathbf{F}^{\text{LO}}}{\partial t} + \frac{c}{3} \nabla E^{\text{LO}} + \sigma_{\text{R}} \mathbf{F}^{\text{LO}} = \gamma^{\text{HO}} c E^{\text{LO}}, \quad (79b)$$

$$\rho c_v \frac{\partial T}{\partial t} + \sigma_{\text{P}} acT^4 - \sigma_{\text{E}}^{\text{HO}} c E^{\text{LO}} = 0, \quad (79c)$$

where

$$\sigma_{\text{E}}^{\text{HO}} \equiv \frac{\int_0^\infty \sigma \int_{4\pi} I^{\text{HO}} d\Omega d\nu}{\int_0^\infty \int_{4\pi} I^{\text{HO}} d\Omega d\nu} = \frac{\sum_{g=1}^G \sigma_g \int_{4\pi} I_g^{\text{HO}} d\Omega}{cE^{\text{HO}}} \quad (80a)$$

is the radiation weighted opacity evaluated from the HO system,

$$\sigma_{\text{P}} \equiv \frac{\int_0^\infty \sigma B(\nu, T) d\nu}{\int_0^\infty B(\nu, T) d\nu} = \sum_{g=1}^G \sigma_g b_g \quad (80b)$$

is the Planck weighted opacity, and

$$\sigma_{\text{R}} = \frac{\int_0^\infty \frac{\partial B}{\partial T} \Big|_T d\nu}{\int_0^\infty \frac{1}{\sigma(\nu, T)} \frac{\partial B}{\partial T} \Big|_T d\nu} = \frac{\sum_{g=1}^G \frac{\partial B_g}{\partial T} \Big|_T}{\sum_{g=1}^G \frac{1}{\sigma_g} \frac{\partial B_g}{\partial T} \Big|_T} \quad (81)$$

is the Rosseland weighted opacity. It is important to note that we use the most up-to-date quantities E^{HO} , I_g^{HO} and b_g to evaluate the weighted opacities, regardless the temporal centering of the multi-frequency opacities σ_g . The solution strategy for the LO system remains the same as described for the gray case, Section 2.1.

We emphasize here that there is a significant advantage of the DP method compared to IMC or S_N for multi-frequency problems in that the particle trajectory, Eq. (29), is independent of frequency and thus all frequency information is carried by each particle. Thus, we can provide the same phase-space resolution with the same number of particles regardless of the number of frequency groups. Although each particle carries more information, and therefore the memory requirements will increase, we can use a single ray-tracing step per particle, thus reducing the computational effort per group.

3. Numerical Results

In the following section, we present multi-dimensional numerical results for the Tophat and Hohlraum problems. One-dimensional demonstrations for the DP method can be found in earlier publications [12, 21].

3.1. Tophat problem

The Tophat, or crooked pipe, problem is a two-dimensional problem in which a region of dense, opaque material ($\rho = 10 \text{ g/cm}^3$, $c_v = 1 \times 10^{12} \text{ erg/g/eV}$, $\sigma = 2000 \text{ cm}^{-1}$) is embedded into a channel of thin material ($\rho = 0.1 \text{ g/cm}^3$, $c_v = 1 \times 10^{12} \text{ erg/g/eV}$, $\sigma = 0.2 \text{ cm}^{-1}$). The channel itself is surrounded by the opaque material. While the original definition was in cylindrical coordinates [9], we have adapted the problem

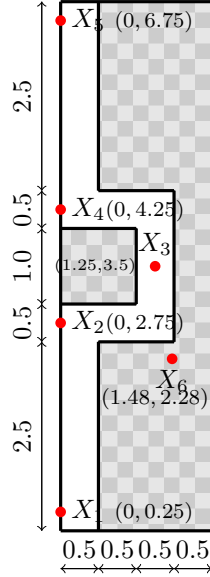


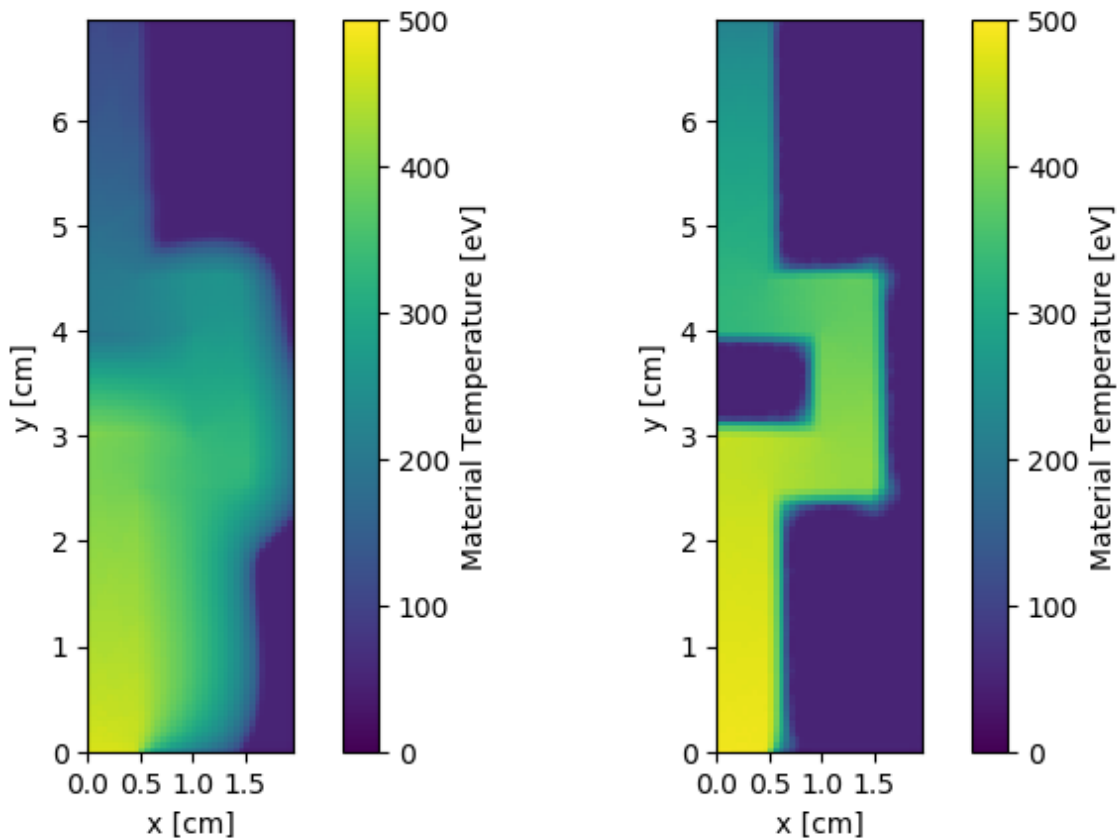
Figure 1 Layout of the Tophat problem, all measurements in cm. The filled areas are the dense material, the rest is optically thin.

to Cartesian coordinates. The problem is 2 cm by 7 cm with a reflective boundary condition at $x = 0$, and vacuum on all other sides. Figure 1 shows the geometry of the problem with the corresponding measurements. The grayed regions contain the opaque material, while the white region is optically thin. The mesh used for the calculation is rectangular with $\Delta x = \Delta y = 0.05$ cm, which gives 40 by 140 cells. In each cell, particles were initialized at the four centers of the corner subcells, using a S_N standard Gauss-Chebyshev product quadrature with 8 polar and 24 azimuthal angles (see Section 2.2.1 for details). This results in a total of 2 150 400 particles.

At the beginning, the problem is in thermal equilibrium at the initial temperature $T_0 = 50$ eV and a temperature source $T_{\text{inc}} = 500$ eV is applied to the bottom of the thin channel at $y = 0$ cm, $x < 0.5$ cm. The problem was run with an initial time step of $\Delta t_0 = 1 \times 10^{-12}$ s, which increased by a factor of 1.1 each step up to a maximum of $\Delta t_{\text{max}} = 5 \times 10^{-11}$ s, for a total time of $t_{\text{end}} = 1 \times 10^{-6}$ s. We used a tolerance of $\tau_{\text{HOLO}} = 1 \times 10^{-4}$ for the HOLO solver with the convergence criteria

$$\frac{\|\mathbf{E}_n^{\text{HO}} - \mathbf{E}_n^{\text{LO}}\|_{\infty}}{\mathbf{E}_n^{\text{LO}}} < \tau_{\text{HOLO}}, \quad (82)$$

$\tau_{\text{P1}} = 1 \times 10^{-8}$ for the P1 solver with the error calculated as the relative infinity norm of the nonlinear Newton-update, and $\tau_T = 1 \times 10^{-12}$ for the temperature solver with the relative Newton-update as error.



(a) Flat source

(b) Linear source

Figure 2 Material temperature for the Tophat problem at 1×10^{-6} s using a square mesh and flat- and linear-source approximations

With time, the radiation travels along the thin channel. The problem cannot be solved accurately with diffusion alone, since diffusion cannot model the flow of radiation around the corners. On the other hand, it is necessary for the algorithm to respect the asymptotic diffusion limit, or the radiation will diffuse too fast into the thick material.

We use six points to track the temperature evolving over time, five in the thin material ($X_1 - X_5$), plus one in the thick material (X_6). The points and their corresponding coordinates are shown in Fig. 1.

The material temperature at the final time 1×10^{-6} s is shown in Fig. 2. These calculations use an orthogonal or square mesh. Fig. 2 clearly shows the effect of

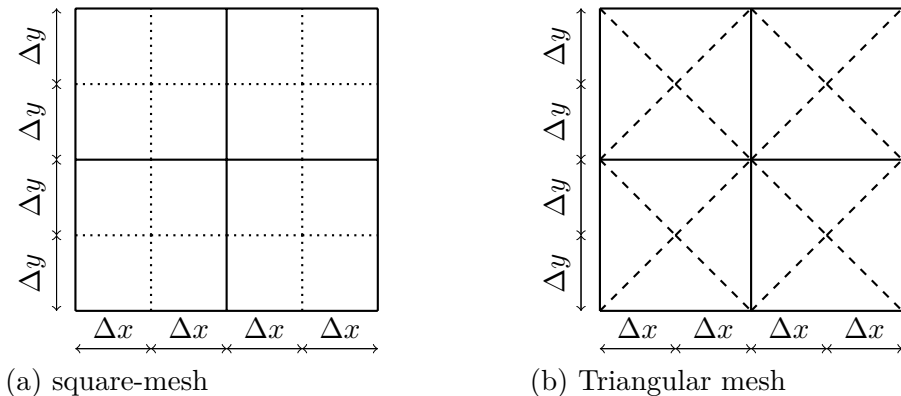


Figure 3 Comparison of part of the square and triangular mesh for the Tophat problem. Dotted lines delimit cells for the square mesh, while dashed delimit cells for the triangular mesh

the linear source approximation. Without a linear source, the radiation diffuses too fast into the thick material (Fig. 2a). Using the linear-source representation, the temperature only heats the first line of cells in the thick material except at the corners of the channel, giving a highly improved solution. The excessive numerical diffusion at the corners is caused by the lack of the bi-linear term in the source shape, which is necessary to recover the asymptotic diffusion limit on rectangular meshes [2]. The error shows preferentially at the corners of the channel, because the linear representation cannot describe the temperature profile sufficiently there.

The linear-source approximation is sufficient for the asymptotic diffusion limit on triangular meshes. To show this, we used a triangular mesh where four cells of the square mesh were combined and then divided into triangles using the center of these four cells as shown in Fig. 3. This approach maintained the number of cells, particles and the area per cell, without introducing any preferred directionality. The results for the flat source do not show any significant change compared to the square mesh (Fig. 4a), however the linear case does not exhibit the excessive numerical diffusion at the corner of the channel (Fig. 4b). This demonstrates that the corner problem is caused by a lack of preservation of the asymptotic limit on the quadrilateral elements.

The time-dependent material temperature for the tracking points is shown in Fig. 5. The further down the channel the tracking point is, the larger is the difference between the flat- and linear-source results (Figs. 5a to 5e), with the flat-source cases showing a much slower increase of temperature. The linear-source cases show also differences between the triangular and the square mesh in regard to how fast the heating occurs. While the square mesh shows faster heating, the final temperature is approximately the same as for the triangular mesh once an equilibrium is reached.

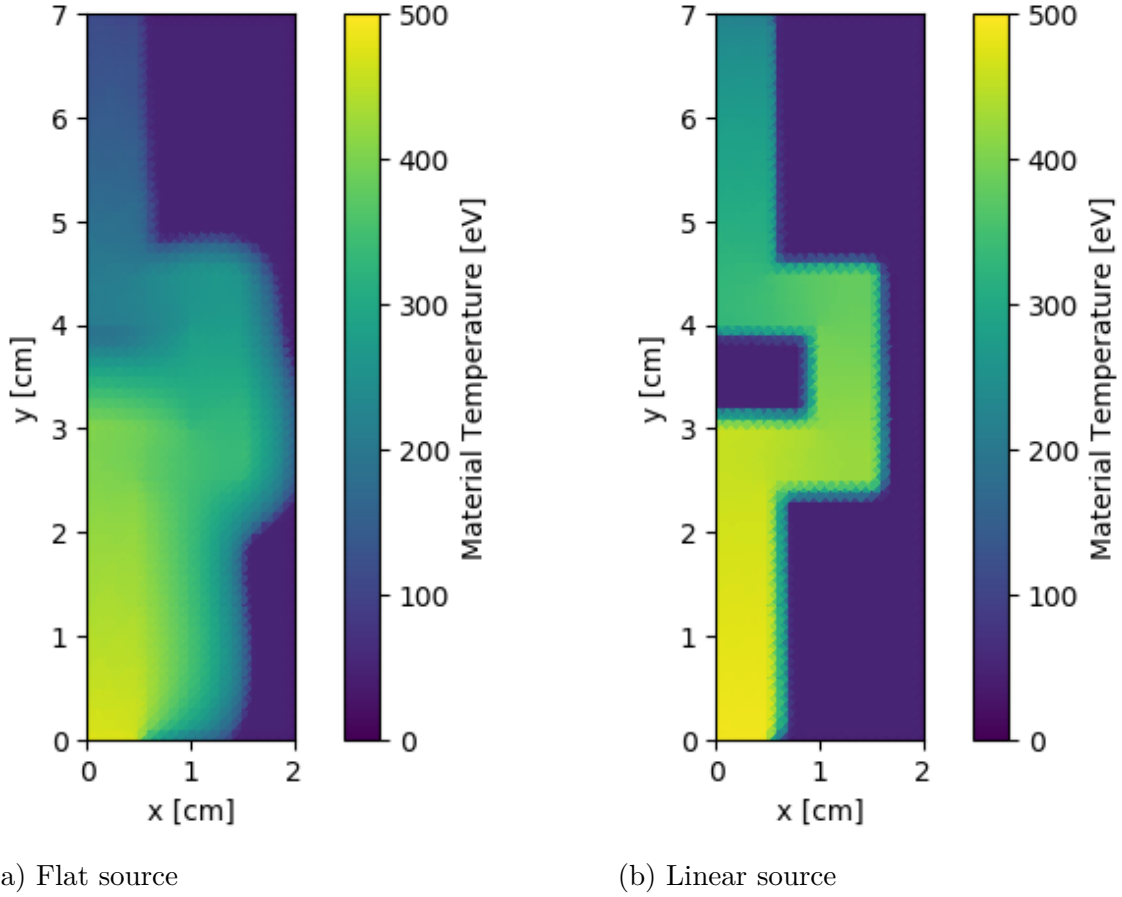
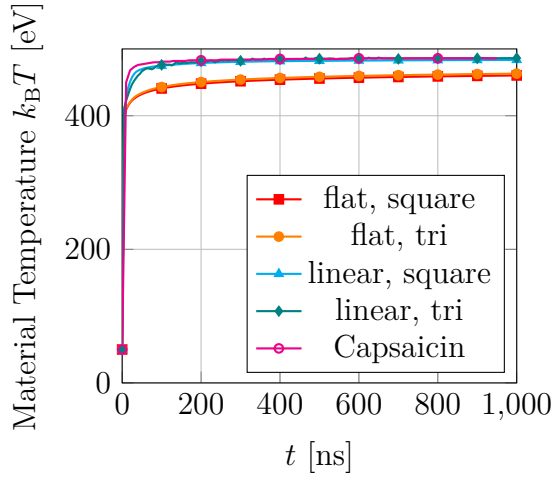


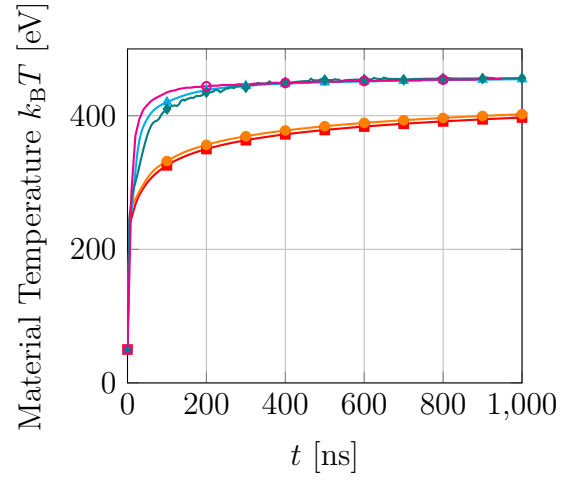
Figure 4 Material temperature for the Tophat problem at 1×10^{-6} s using a triangular sub-mesh and flat- and linear-source approximations

The results for X_6 (Fig. 5f) show the material temperature away from the channel at a corner. It confirms the previous finding with regard to the diffusion limit. The cases using a flat-source approximation show a strong increase of the material temperature. The linear-source case on the square mesh also shows an increase in the temperature for later times, but it is significantly smaller than for the flat-source cases. The linear-source case on the triangular mesh, preserving the asymptotic diffusion limit, shows no increase at all for point X_6 .

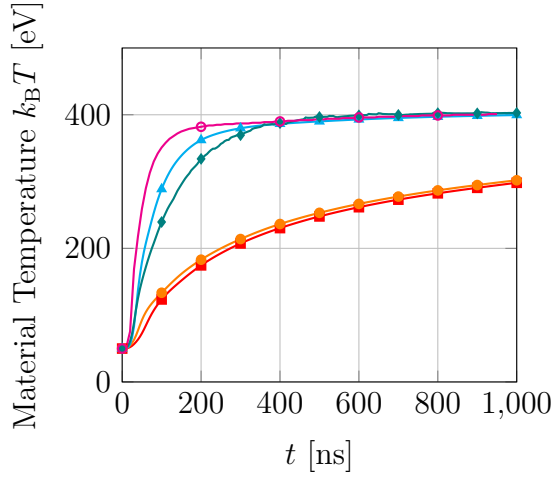
We have compared our results to Capsaicin [24]. Capsaicin shows faster transients than our code with the linear source, especially for points X_4 and X_5 . But both codes show the same asymptotic solution for later times. The differences in the transients arise from the mesh, which is not sufficiently refined to resolve the boundary layer at



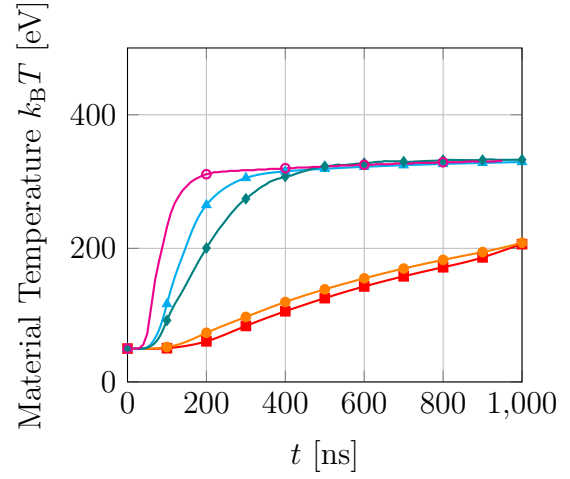
(a) Point X_1



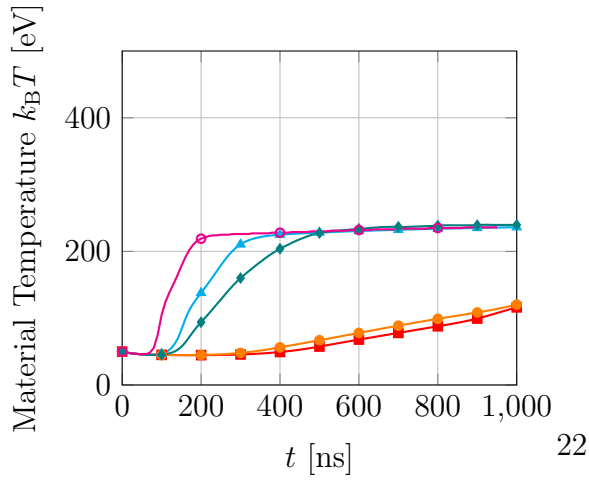
(b) Point X_2



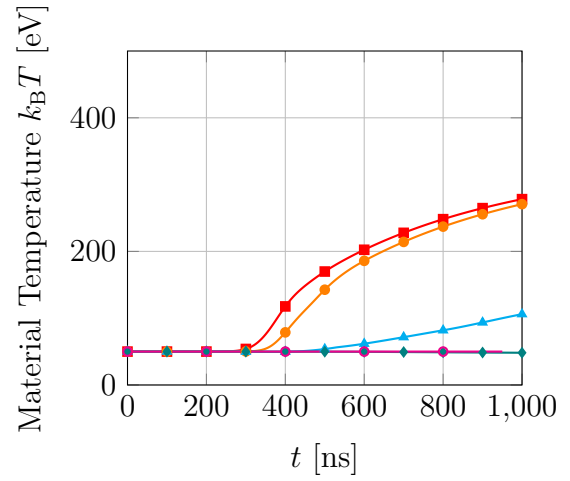
(c) Point X_3



(d) Point X_4



(e) Point X_5



(f) Point X_6

Figure 5 Material temperature over time for the six tracking points in the Tophat problem.

the interface between the channel and the thick material.

3.2. Hohlraum problem

The second problem we present in this paper is the heating of a cavity from a radiation source. Similar problems have been studied in literature [16, 3], but with different geometry and materials. The layout is shown in Fig. 6. The problem is 0.65 cm by 1.4 cm, with a square mesh of 39×84 cells. The walls of the cavity have a frequency-dependent opacity

$$\sigma(\nu, T) = \rho\alpha \frac{1 - e^{-\frac{h\nu}{k_B T}}}{(h\nu)^3}, \quad (83)$$

with the opacity factor $\alpha = 1 \times 10^{12} \text{ eV}^3 \text{ cm}^2 \text{ g}^{-1}$, density $\rho = 1.0 \text{ g cm}^{-3}$ and the heat capacity $c_v = 3 \times 10^{12} \text{ erg/g/eV}$, while the cavity is filled with a material that is almost a vacuum ($\rho = 1 \times 10^{-3} \text{ g cm}^{-3}$, $c_v = 1 \times 10^{12} \text{ erg/g/eV}$) and highly transparent ($\sigma = 1 \times 10^{-8} \text{ cm}^{-1}$). The frequency was discretized into 100 uniform, logarithmic groups between $\nu_{\min} = 1 \times 10^{-3} \text{ eV}$ and $\nu_{\max} = 1 \times 10^6 \text{ eV}$. The left side of the problem has a reflective boundary condition, all other sides are vacuum conditions. At the beginning, the problem is in thermal equilibrium at $T_0 = 1.0 \text{ eV}$, with the temperature at $y = 0 \text{ cm}$ set to $T_{\text{inc}} = 300 \text{ eV}$. The problem was run with an initial time step of $\Delta t_0 = 1 \times 10^{-12} \text{ s}$, increased by a factor of 1.1 each step up to a maximum of $\Delta t_{\max} = 5 \times 10^{-12} \text{ s}$, for a total time of $t_{\text{end}} = 1 \times 10^{-8} \text{ s}$. We used a tolerance of $\tau_{\text{HOLO}} = 1 \times 10^{-4}$ for the HOLO solver, $\tau_{\text{P1}} = 1 \times 10^{-8}$ for the P1 solver and $\tau_T = 1 \times 10^{-12}$ for the temperature solver.

The radiation temperature at $t = 1 \times 10^{-8} \text{ s}$ is shown in Fig. 7a using a standard S_N Gauss-Chebyshev product quadrature with 8 polar and 24 azimuthal angles. This quadrature results a total number of 1 257 984 particles used in the calculation, where we initialize 4 particles per cell. Note that the number of particles remains constant once initialized, as no particles are killed or created during the calculation. The plot clearly shows ray effects, with heating preferentially occurring along directions included in the quadrature set, while the temperature between these directions stays unphysically cold. They can be seen especially well in the upper region, where the wall sees only a highly localized deposition of energy (as shown by the material temperature in Fig. 8a), whereas it should be a much wider deposition on the part that is not shadowed. The lower wall shows a smooth material temperature profile, while the lower side of the center block already shows indications of ray effects with localized temperature extrema.

It is customary not to include the axis of the coordinate system in S_N quadrature sets. However, having a quadrature set that is axis-aligned improves the results at the top wall as shown in Fig. 7b. The axis aligned quadrature has 9 polar angles and

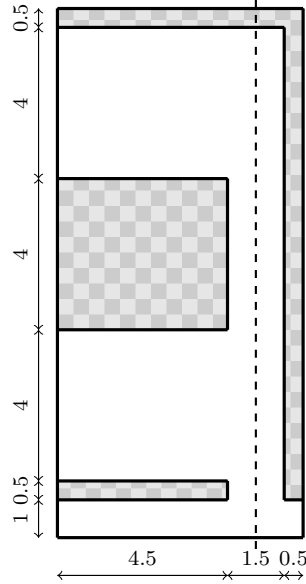
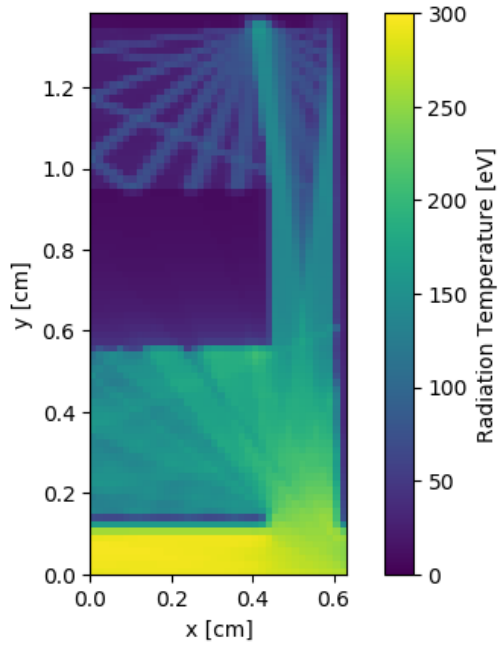


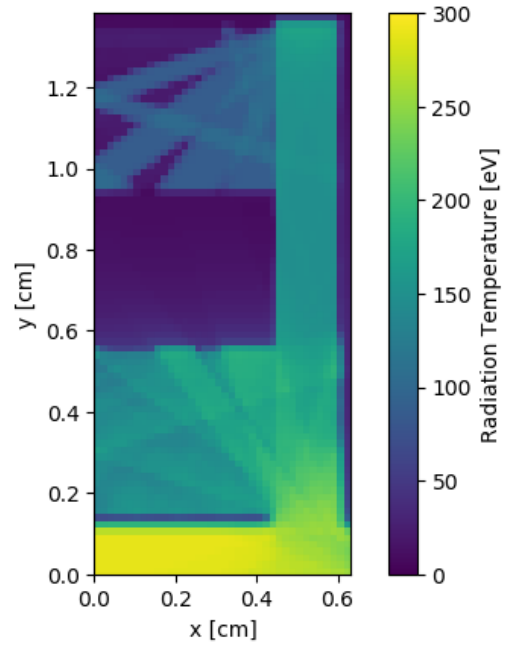
Figure 6 Layout of the Hohlraum problem. All measurements are in mm. The filled areas are the dense material, the rest are optically thin.

20 azimuthal angles, which results in a total of 1 310 400 particles. We chose these settings to be closer to the total number of angles of the standard Gauss-Chebyshev quadrature, and to avoid 45° angles, which cause many particles to hit the corners of the square-mesh cells. While our implementation is capable of handling particles hitting cell corners, it fails for large numbers of particles because the corner case is highly ill-conditioned due to very short particle tracks. Even though the axis-aligned quadrature improves the results for the top wall, we still see strong ray effects.

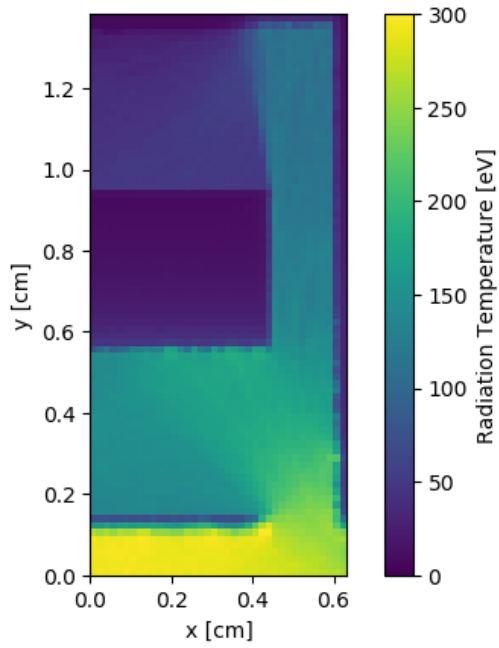
To further ameliorate this problem, we switched to a random quadrature with a total number of 96 angles (which is the same as for the Gauss-Chebyshev quadrature, since we are two-dimensional). These random angles are different for each particle starting point (4 per cell). After the particles are initialized, they maintain their direction, except when they are reflected at a boundary by the reflection law Eq. (37). This approach results in a lot more angles covered by the particles, but introduces random noise. The radiation temperature does not show ray-effects, and a smooth radiation field develops in the optically thin material, as can be seen in Fig. 7c. However, we see strong differences in the thick material between neighboring cells caused by noise. The material temperature in Fig. 8c shows this well for the lower wall. Note that the HOLO solver did not converge for the random quadrature case due to abrupt changes in particle surface fluxes when particles cross cells, stalling after



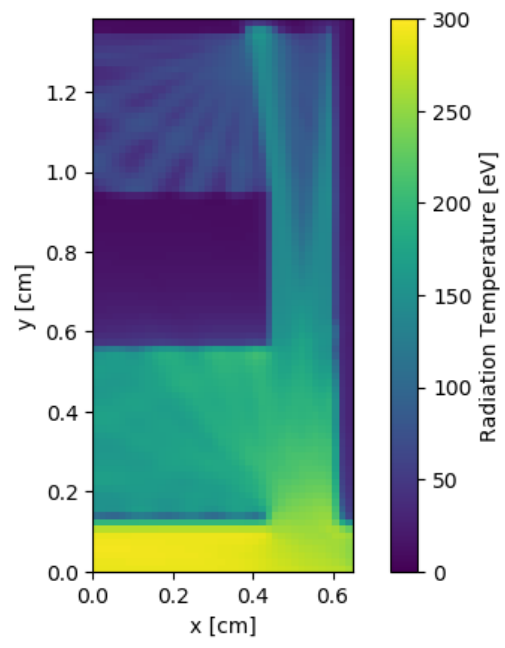
(a) Gauss



(b) Axis aligned

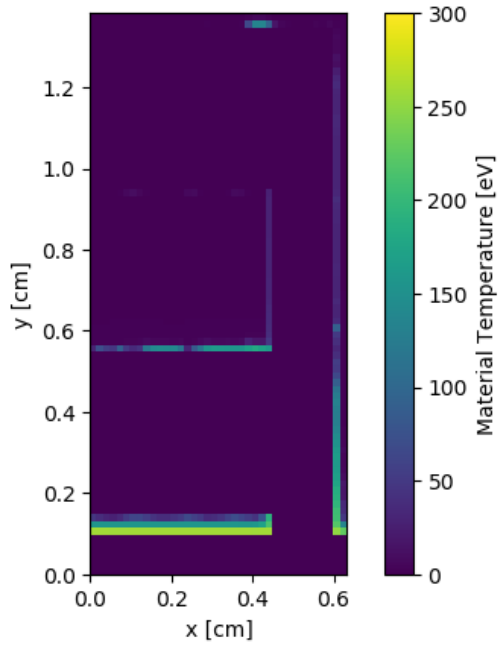


(c) Random

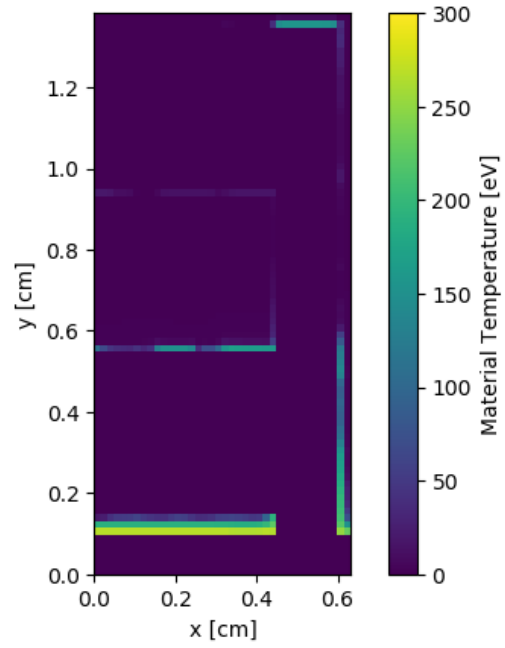


(d) Capsaicin

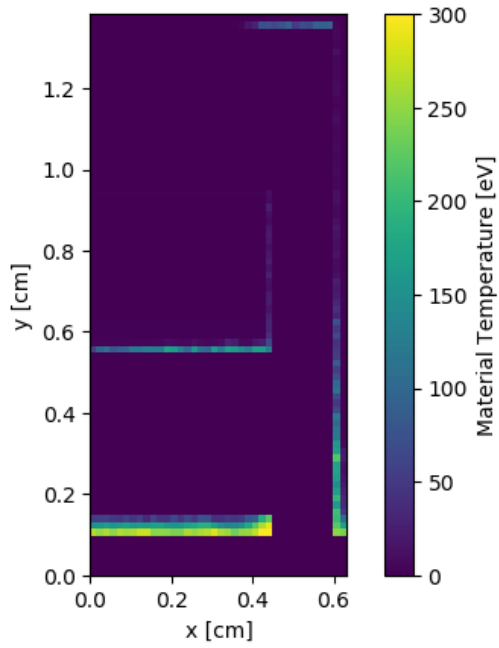
Figure 7 Radiation temperature for the Hohlraum problem at 1×10^{-8} s using the different quadrature types.



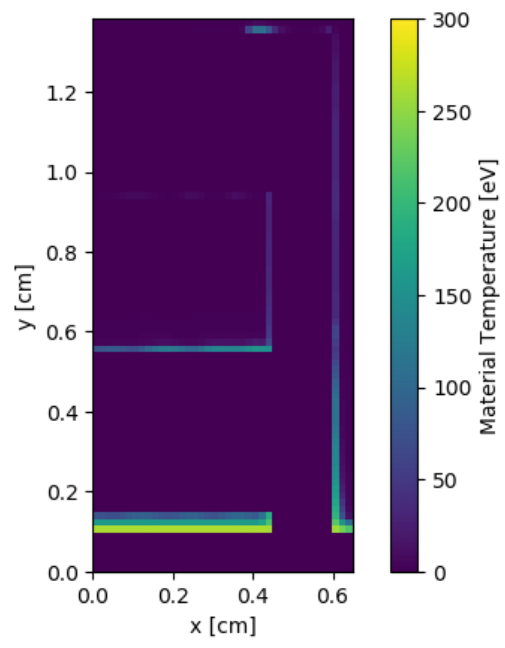
(a) Gauss



(b) Axis Aligned



(c) Random



(d) Capsaicin

Figure 8 Material temperature for the Hohlraum problem at 1×10^{-8} s using the different quadrature types.

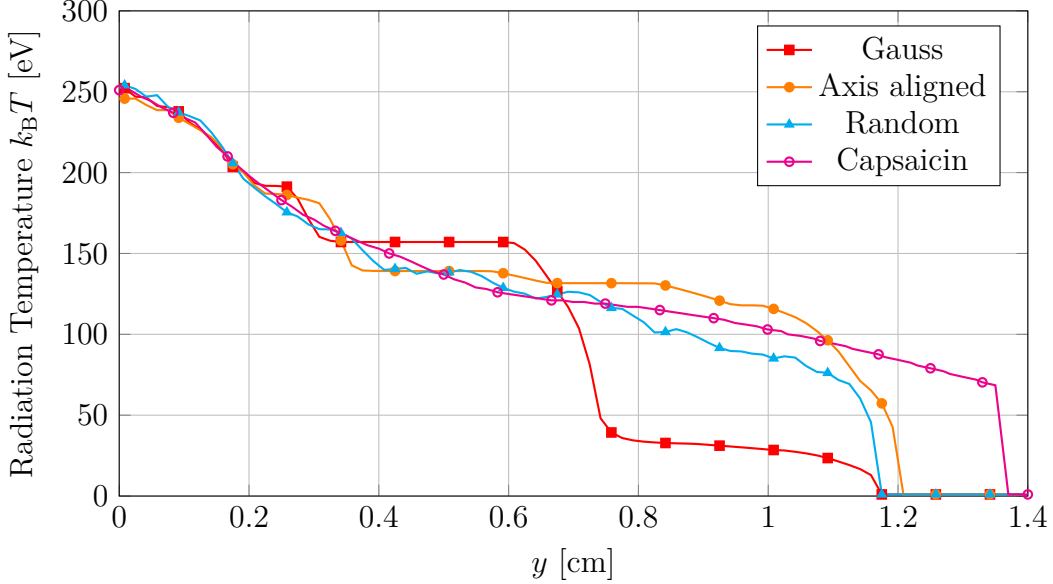


Figure 9 Radiation wave front at $x = 0.525$ cm at time $t = 4 \times 10^{-11}$ s using a constant time step size $dt = 1 \times 10^{-11}$ s.

about two iterations at a residual magnitude of approximately 1×10^{-2} . Therefore we limited the number of HOLO iterations to 5 per time step for the random cases. A test with an increased number of particles per cell showed a significantly improved HOLO convergence. Future work will explore higher-order particle interpolation to ameliorate this problem.

The results obtained with Capsaicin [24] are shown in Figs. 7d and 8d. We see good agreement for the radiation temperature in the optically thin material between Capsaicin and the standard Gauss-Chebyshev quadrature, Fig. 7a. The ray effects are more smeared out in Capsaicin but clearly visible. The material temperature was higher and more evenly distributed in the upper part of the bottom wall. We believe these differences are caused by Capsaicin's linearization of the T^4 nonlinearity in the emission source.

Figure 9 shows the radiation wave front at the time $t = 4 \times 10^{-11}$ s along the dashed line in Fig. 6. The exact location should be $ct = 1.1991$ cm. The results show that our code is within reasonable range of this analytical value. Deviations from this value come from the different angles contained in the quadrature used, i.e., the Gauss quadrature has no direction going perpendicular to the wave front, which results in a slower propagation. The steps in the temperature profile for both the Gauss quadrature and the axis-aligned quadrature are related to the discrete propagation

angles considered. The Capsaicin wave front has propagated much further compared to both our results and the analytical value, a consequence of the backward Euler time discretization introducing excessive numerical diffusion.

3.3. Runtime and Convergence

To control the runtime necessary for the convergence studies, we limited our study to the one-dimensional Marshak-wave problem. The implementation is the same as in two dimensions.

The Marshak-wave problem propagates a radiation wave through a material with a temperature dependent opacity

$$\sigma(T) = \frac{\rho\alpha}{T^3} \quad (84)$$

with the opacity factor $\alpha = 1 \times 10^6 \text{ eV}^3 \text{ cm}^2 \text{ g}^{-1}$. The problem is 2 cm long divided into n mesh cells, with vacuum boundaries on both sides. In the beginning, the problem is in thermal equilibrium at $T_0 = 0.025 \text{ eV}$, and on the left side a temperature of $T_{\text{inc}} = 150 \text{ eV}$ is applied. The problem was run with an initial time step of $\Delta t_0 = 1 \times 10^{-12} \text{ s}$, which increased by a factor of 1.1 each step up to a prescribed maximum Δt_{max} , for a total time of $t_{\text{end}} = 5 \times 10^{-8} \text{ s}$.

The total runtime is a function of the maximum time step size Δt_{max} , as shown in Fig. 10 for different mesh sizes. There are three major effects influencing the runtime. The first factor is the number of time steps required to reach the final time, which decreases inversely with increasing Δt_{max} . The second is the number of cells a particle crosses on average during one time step, which increases proportionally with the time step size. The last is the number of HOLO iterations necessary to converge the residual. This number increases for large time step sizes, while it remains almost constant for small ones. The combination of these leads to an optimal time step size for which the total run time is minimal. Figure 10 shows that this optimum can be found for different mesh sizes for an almost constant ratio of $c\Delta t_{\text{max}}/\Delta x$, corresponding to a maximum number of cells crossings between 100 and 300. The actual number of cells crossings is a function of the particle's direction.

While the method is stable for large time steps [21], there are upper and lower limits to consider. If the time step is too small, no particle crosses the cell surfaces. This results in zero fluxes for the LO solver, and a decoupling of the cells. This can also occur in a later time step due to alignment of the particles resulting in no surface crossings. The upper time step limit is imposed by the dynamical time scale. If the time step size is too large, the wave front stalls as shown in Fig. 11. For $\Delta t_{\text{max}} \leq 2 \times 10^{-11} \text{ s}$, or $c\Delta t_{\text{max}}/\Delta x \lesssim 480$, the wave front reaches the correct final

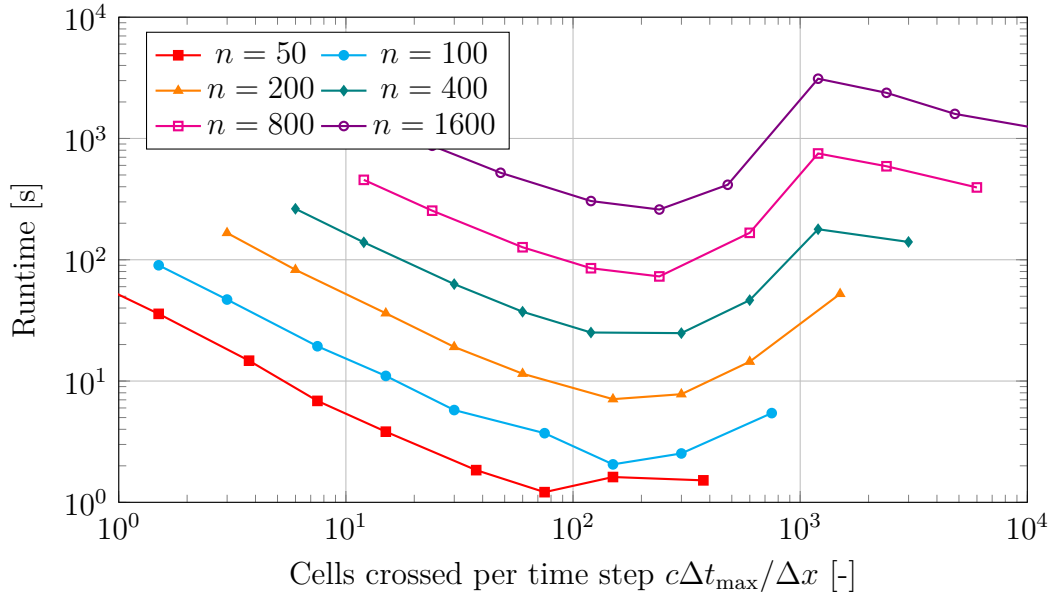


Figure 10 Runtime as a function of maximal number of cells crossed per time step $c\Delta t_{\max}/\Delta x$ for different mesh sizes n .

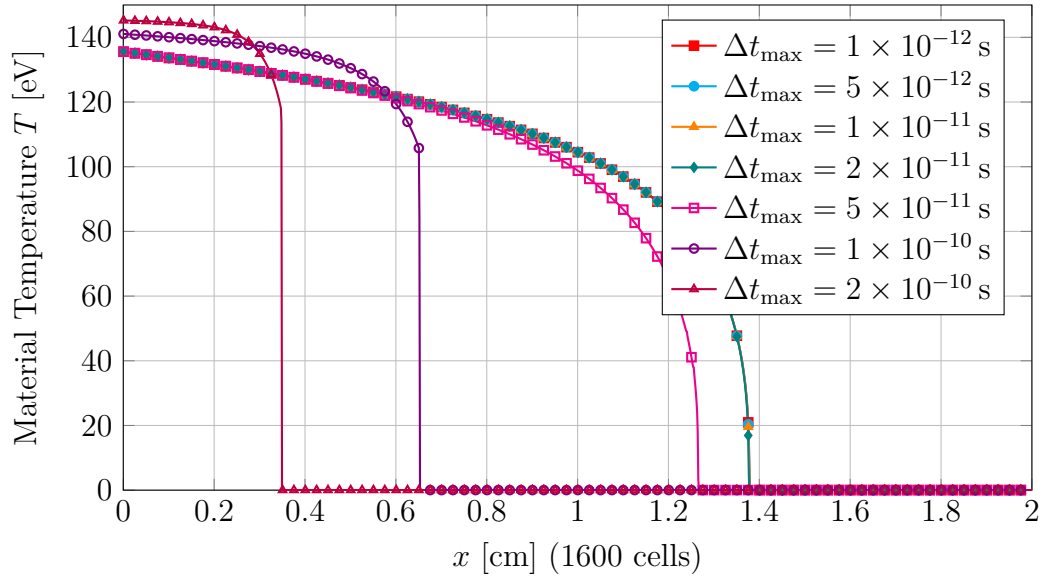


Figure 11 Results for the thin Marshak wave at $t = 5 \times 10^{-8}$ s using different Δt_{\max} and a mesh with 1600 cells.

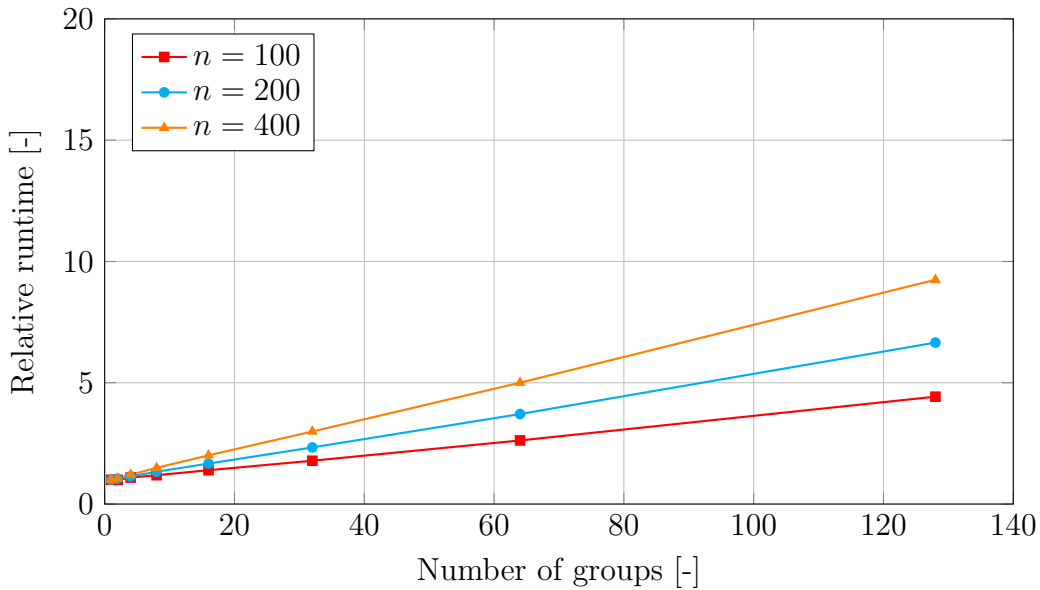


Figure 12 Runtime as a function of number of groups for different numbers of mesh cells n .

position, but for larger time steps the final position of the wave front lags behind. We observed the same value of the time step threshold for different meshes.

The DP method is very well suited for multi-frequency calculations as mentioned before. All frequency information is carried by each particle, and the group iteration is the innermost loop during the tracking step. Therefore, the runtime is proportional to the number of frequency groups with a factor significantly less than unity. Figure 12 shows the runtime of the Marshak wave problem as a function of group number for several mesh sizes using $\Delta t_{\max} = 1 \times 10^{-12}$ s. The slope is dependent on the ratio of work done within the inner loop to the work outside of it. A finer mesh results in more cell crossings, increasing the ratio and hence increasing the slope. However, the slope will always remain less than unity.

We present next results on the convergence properties of the algorithm. To reduce the runtime for the convergence studies, we limited the simulation time to $t_{\text{end}} = 2 \times 10^{-9}$ s, and the problem size to 1 cm. To avoid problems with the upper time step-size limit, we used a time step of $\Delta t = 1 \times 10^{-12}$ s. For the spatial convergence, we use a mesh with $n = 3200$ cells as reference to calculate the error. The results shown in Fig. 13 indicate an approximately first-order convergence rate with spatial refinement. The convergence in angle is second order, as can be seen in Fig. 14, where the reference solution used $M_P = 64$ polar angles. Figure 15 shows the convergence with the number of particle starting points per cell (each point uses all directions

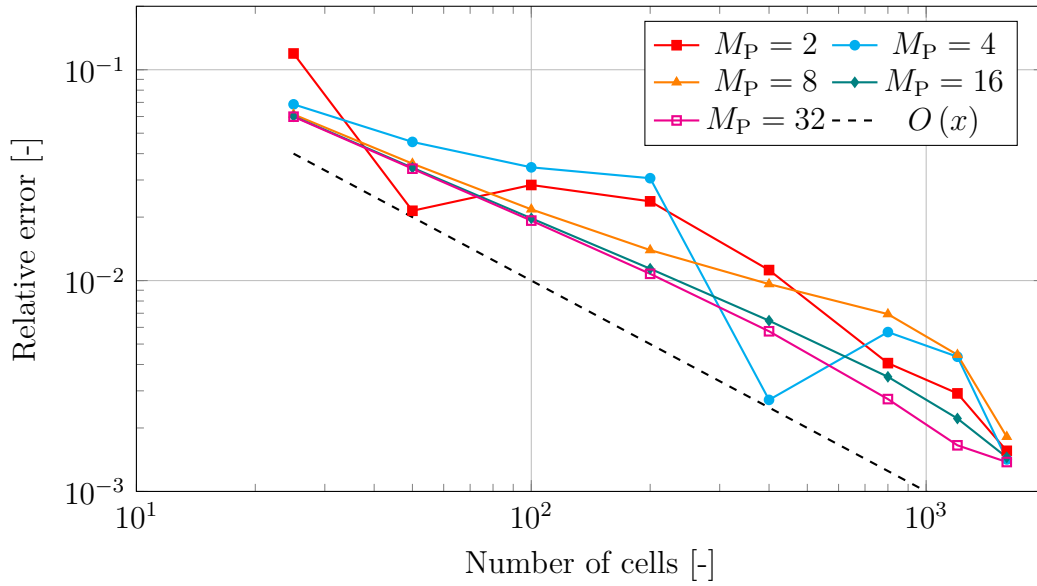


Figure 13 Error convergence with the number of mesh cells for different number of polar angles M_P .

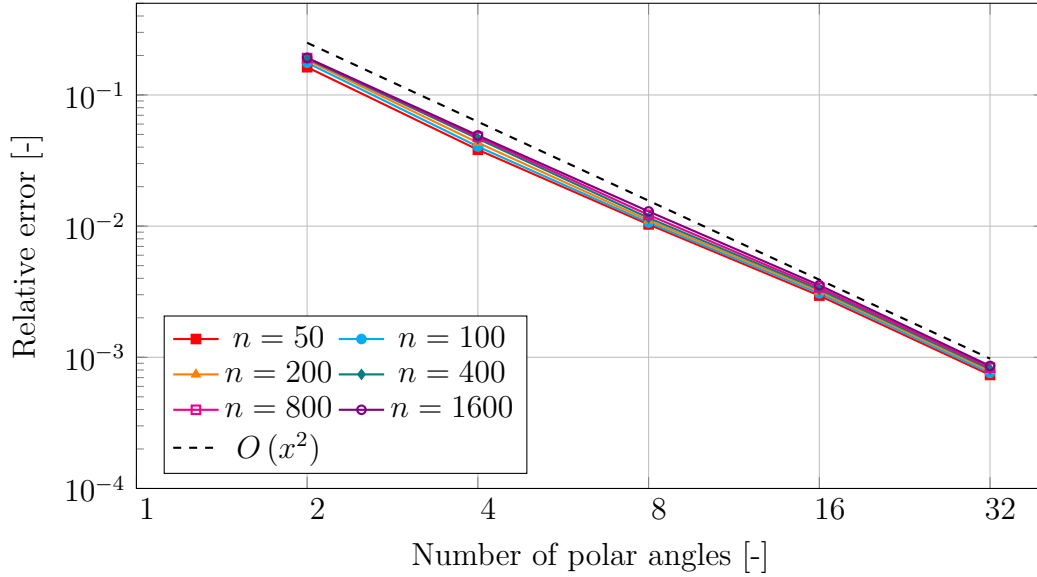


Figure 14 Error convergence with the number of polar angles for different number of mesh cells n .

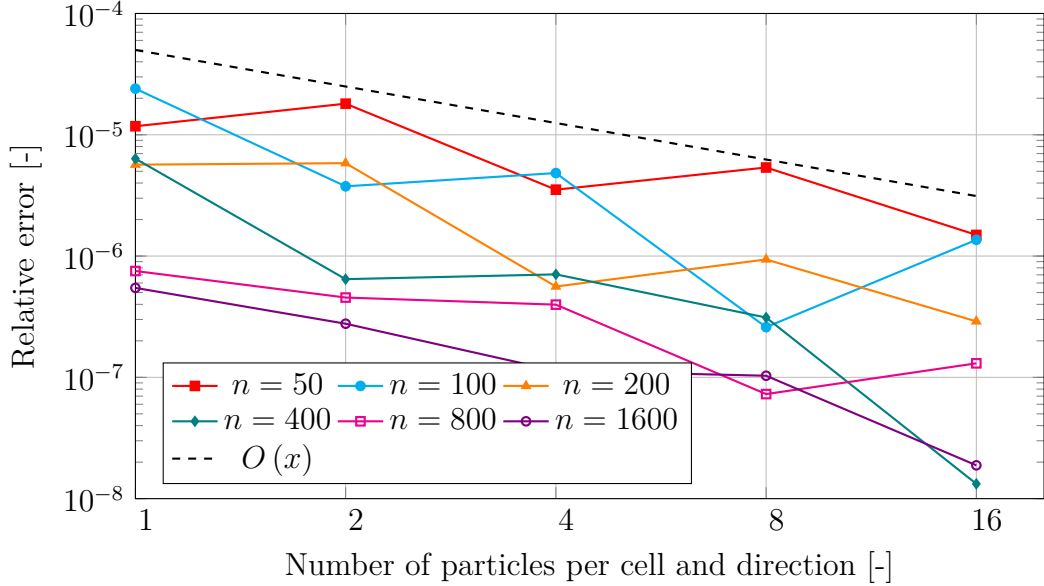


Figure 15 Error convergence with the number of particle starting points per cell with 32 polar angles per point and different number of mesh cells n .

of the angular quadrature). The error with respect to a reference solution using 32 starting points is much lower than for the other cases, Figs. 13 and 14, and converges with first order. However, there seem to be some fluctuations.

4. Conclusion

We have extended the moment accelerated, multi-frequency deterministic particle method proposed by Park et al. [21] to two dimensional thermal radiative transfer problems using a fast ray-tracing algorithm. A linear reconstruction of the emission source, obtained from a discretely consistent, moment-based low-order solver, allows the analytical integration of the characteristic equation along a particle track, resulting in an improved solution in optically thick materials compared to other particle methods. In contrast to Monte-Carlo (MC) methods, our method does not feature randomness (with the possible exception of particle initialization and random quadrature to ameliorate ray effects), therefore the solution does not contain stochastic noise. We showed how we can obtain a linear reconstruction of the energy deposition, material temperature and emission source using spatial moments. With this, we were able to demonstrate that our HO system features the asymptotic diffusion limit, at least on triangular meshes.

We further showed that, using the flexibility of a particle method, we can reduce ray-effects by using random quadrature sets, but it introduces noise in the solution.

Future work will include the implementation of a bi-linear source reconstruction for rectangular meshes, the development of a DG discretization scheme for the LO system, which self-consistently solves for the LO slope, and the extension to cylindrical geometries.

5. Acknowledgment

This work was supported by the US Department of Energy through the Los Alamos National Laboratory. Los Alamos National Laboratory is operated by Triad National Security, LLC, for the National Nuclear Security Administration of U.S. Department of Energy (Contract No. 89233218CNA000001). Research presented in this article was supported by the Laboratory Directed Research and Development program of Los Alamos National Laboratory under project number 20160448ER.

6. References

References

- [1] Marvin L. Adams. Discontinuous Finite Element Transport Solutions in Thick Diffusive Problems. *Nuclear Science and Engineering*, 137(3):298–333, March 2001. ISSN 0029-5639. doi: 10.13182/NSE00-41. URL <https://doi.org/10.13182/NSE00-41>.
- [2] Marvin L. Adams, Todd A. Wareing, and Wallace F. Walters. Characteristic Methods in Thick Diffusive Problems. *Nuclear Science and Engineering*, 130(1):18–46, September 1998. ISSN 0029-5639. doi: 10.13182/NSE98-A1987. URL <https://doi.org/10.13182/NSE98-A1987>.
- [3] Thomas A Brunner. Forms of Approximate Radiation Transport. Technical Report SAND2002-1778, 800993, Sandia National Laboratories, Albuquerque, NM (United States), June 2002. URL <http://www.osti.gov/servlets/purl/800993/>.
- [4] L. Chacón, G. Chen, D. A. Knoll, C. Newman, H. Park, W. Taitano, J. A. Willert, and G. Womeldorff. Multiscale high-order/low-order (HOLO) algorithms and applications. *Journal of Computational Physics*, 330:21–45, February 2017. ISSN 0021-9991. doi: 10.1016/j.jcp.2016.10.069. URL <http://www.sciencedirect.com/science/article/pii/S0021999116305770>.

- [5] R. Ferrer, J. Rhodes, and K. Smith. Linear source approximation in CASMO5. In *PHYSOR 2012 - Advances in Reactor Physics - Linking Research, Industry and Education*, Knoxville, TN, April 2012. American Nuclear Society. URL http://inis.iaea.org/Search/search.aspx?orig_q=RN:44063435.
- [6] Rodolfo M. Ferrer and Joel D. Rhodes III. A Linear Source Approximation Scheme for the Method of Characteristics. *Nuclear Science and Engineering*, 182(2):151–165, February 2016. ISSN 0029-5639. doi: 10.13182/NSE15-6. URL <https://doi.org/10.13182/NSE15-6>.
- [7] Rodolfo M. Ferrer and Joel D. Rhodes III. The linear source approximation and particle conservation in the Method of Characteristics for isotropic and anisotropic sources. *Annals of Nuclear Energy*, 115:209–219, May 2018. ISSN 0306-4549. doi: 10.1016/j.anucene.2018.01.023. URL <https://www.sciencedirect.com/science/article/pii/S0306454918300203>.
- [8] J. A. Fleck and J. D. Cummings. An implicit Monte Carlo scheme for calculating time and frequency dependent nonlinear radiation transport. *Journal of Computational Physics*, 8(3):313–342, December 1971. ISSN 0021-9991. doi: 10.1016/0021-9991(71)90015-5. URL <http://www.sciencedirect.com/science/article/pii/0021999171900155>.
- [9] N. A. Gentile. Implicit Monte Carlo Diffusion—An Acceleration Method for Monte Carlo Time-Dependent Radiative Transfer Simulations. *Journal of Computational Physics*, 172(2):543–571, September 2001. ISSN 0021-9991. doi: 10.1006/jcph.2001.6836. URL <http://www.sciencedirect.com/science/article/pii/S0021999101968366>.
- [10] Andrew S. Glassner. *An Introduction to Ray Tracing*. Elsevier, June 1989. ISBN 978-0-08-049905-5.
- [11] V. Ya. Gol’din. A quasi-diffusion method of solving the kinetic equation. *USSR Computational Mathematics and Mathematical Physics*, 4(6):136–149, January 1964. ISSN 00415553. doi: 10.1016/0041-5553(64)90085-0. URL <http://linkinghub.elsevier.com/retrieve/pii/0041555364900850>.
- [12] Hans Hammer, HyeongKae Park, and Luis Chacón. A multi-dimensional, moment-accelerated deterministic particle method for time-dependent thermal radiative transfer problems. In *ANS Annual Winter Meeting 2018*, Orlando, Florida, November 2018. ANS.

- [13] E. W. Larsen, G. C. Pomraning, and V. C. Badham. Asymptotic analysis of radiative transfer problems. *Journal of Quantitative Spectroscopy and Radiative Transfer*, 29(4):285–310, April 1983. ISSN 0022-4073. doi: 10.1016/0022-4073(83)90048-1. URL <http://www.sciencedirect.com/science/article/pii/0022407383900481>.
- [14] Edward W Larsen and J. E. Morel. Asymptotic solutions of numerical transport problems in optically thick, diffusive regimes II. *Journal of Computational Physics*, 83(1):212–236, July 1989. ISSN 0021-9991. doi: 10.1016/0021-9991(89)90229-5. URL <http://www.sciencedirect.com/science/article/pii/0021999189902295>.
- [15] Edward W Larsen, J. E Morel, and Warren F Miller Jr. Asymptotic solutions of numerical transport problems in optically thick, diffusive regimes. *Journal of Computational Physics*, 69(2):283–324, April 1987. ISSN 0021-9991. doi: 10.1016/0021-9991(87)90170-7. URL <http://www.sciencedirect.com/science/article/pii/0021999187901707>.
- [16] Ryan G. McClarren and Cory D. Hauck. Robust and accurate filtered spherical harmonics expansions for radiative transfer. *Journal of Computational Physics*, 229(16):5597–5614, August 2010. ISSN 0021-9991. doi: 10.1016/j.jcp.2010.03.043. URL <http://www.sciencedirect.com/science/article/pii/S0021999110001622>.
- [17] T. M. Pandya and M. L. Adams. Method of long characteristics applied in space and time. In *International Conference on Mathematics, Computational Methods & Reactor Physics (M&C 2009)*, Saratoga Springs, NY, May 2009.
- [18] Tara M. Pandya, Marvin L. Adams, and W. Daryl Hawkins. Long characteristics with piecewise linear sources designed for unstructured grids. In *International Conference on Mathematics and Computational Methods Applied to Nuclear Science and Engineering (M&C 2011)*, Rio de Janeiro, RJ, Brazil, May 2011. Latin American Section (LAS) / American Nuclear Society (ANS). ISBN 978-85-63688-00-2. URL http://inis.iaea.org/Search/search.aspx?orig_q=RN:48022307.
- [19] H. Park, D. A. Knoll, R. M. Rauenzahn, A. B. Wollaber, and J. D. Densmore. A Consistent, Moment-Based, Multiscale Solution Approach for Thermal Radiative Transfer Problems. *Transport Theory and Statistical Physics*, 41(3-4):284–303, May 2012. ISSN 0041-1450. doi: 10.1080/00411450.2012.671224. URL <http://dx.doi.org/10.1080/00411450.2012.671224>.

- [20] H. Park, D. Knoll, R. Rauenzahn, C. Newman, J. Densmore, and A. Wollaber. An Efficient and Time Accurate, Moment-Based Scale-Bridging Algorithm for Thermal Radiative Transfer Problems. *SIAM Journal on Scientific Computing*, 35(5):S18–S41, January 2013. ISSN 1064-8275. doi: 10.1137/120881075. URL <http://epubs.siam.org/doi/abs/10.1137/120881075>.
- [21] H. Park, L. Chacón, A. Matsekh, and G. Chen. A Multigroup Moment-Accelerated Deterministic Particle Solver for Time-dependent Thermal Radiative Transfer Problems. *arXiv:1901.05454 [physics]*, January 2019. URL <http://arxiv.org/abs/1901.05454>.
- [22] HyeonKae Park, Luis Chacón, Anna Matsekh, Guangye Chen, and Hans Hammer. Multigroup Deterministic Particle Solver for 1D Curvilinear Geometries. In *ANS Annual Winter Meeting 2018*, Orlanda, Florida, November 2018. ANS.
- [23] Carsten Steger. On the calculation of moments of polygons. Technical report, Technical Report FGBV–96–04, Forschungsgruppe Bildverstehen (FG BV), Informatik IX, Technische Universität München, 1996.
- [24] Kelly G. Thompson, James S. Warsa, Kent G Budge, and Jae H Chang. Capsaicin: Deterministic Thermal Radiative Transfer. Technical Report LA-UR-06-3387, Los Alamos National Laboratory, Los Alamos, NM, USA, May 2006.
- [25] Ryan T. Wollaeger, Allan B. Wollaber, Todd J. Urbatsch, and Jeffrey D. Densmore. Implicit Monte Carlo with a Linear Discontinuous Finite Element Material Solution and Piecewise Non-Constant Opacity. *Journal of Computational and Theoretical Transport*, 45(1-2):123–157, February 2016. ISSN 2332-4309. doi: 10.1080/23324309.2016.1157491. URL <https://doi.org/10.1080/23324309.2016.1157491>.
- [26] B. C. Yee, A. B. Wollaber, T. S. Haut, and H. Park. A Stable 1D Multigroup High-Order Low-Order Method. *Journal of Computational and Theoretical Transport*, 46(1):46–76, July 2017. ISSN 2332-4309. doi: 10.1080/23324309.2016.1187172. URL <https://doi.org/10.1080/23324309.2016.1187172>.

A. Appendix

A.1. Low-Order solution strategy

The LO system is solved using a Newton-Krylov method with nonlinear elimination [19]. Given an iterate for the radiation energy density $\bar{E}_{i,n,\ell}$ at LO iteration ℓ , the

radiative flux can be calculated from

$$\bar{F}_{j,n,\ell+1} = \frac{1}{\frac{1}{c\Delta t_n} + \sigma_{j,n}} \left(\left(\gamma_{j,n}^+ + \frac{1}{3\Delta x_j} \right) c\bar{E}_{j-\frac{1}{2},n,\ell} - \left(\gamma_{j,n}^- + \frac{1}{3\Delta x_j} \right) c\bar{E}_{j+\frac{1}{2},n,\ell} + \frac{\bar{F}_{j,n-1}}{c\Delta t_n} \right) \quad (85)$$

and the material temperature

$$\rho c_v \frac{T_{i,n,\ell+1} - T_{i,n-1}}{\Delta t_n} + \sigma_{i,n} acT_{i,n,\ell+1}^4 - \sigma_{i,n} c\bar{E}_{i,n,\ell} = 0. \quad (86)$$

using a cell-wise Newton solve. With the new iterates, we can update the radiation energy density with a Newton-Krylov step. The residual vector $\mathbf{R}_{n,\ell+1}$

$$R_{i,n,\ell+1} = \frac{\bar{E}_{i,n,\ell} - \bar{E}_{i,n-1}}{\Delta t_n} + \sum_{j \in i} \hat{\mathbf{n}}_{ij} \cdot \hat{\mathbf{n}}_j \frac{\bar{F}_{j,n,\ell+1} A_j}{V_i} + \sigma_{i,n} c\bar{E}_{i,n,\ell} - \sigma_{i,n} acT_{i,n,\ell+1}^4 - \mathcal{R}_{i,n} \quad (87a)$$

is used to solve for the Newton update

$$\delta_{n,\ell+1} = -\tilde{\mathbb{J}}_{n,\ell+1}^{-1} \mathbf{R}_{n,\ell+1} \quad (87b)$$

and to update the solution vector for the radiation energy density

$$\mathbf{E}_{n,\ell+1} = \mathbf{E}_{n,\ell} + \delta_{n,\ell+1}. \quad (87c)$$

The Jacobian in Eq. (87b) is given by

$$\tilde{\mathbb{J}} = \mathbb{J}_{EE} - \mathbb{J}_{ET} \mathbb{J}_{TT}^{-1} \mathbb{J}_{TE} - \mathbb{J}_{EF} \mathbb{J}_{FF}^{-1} \mathbb{J}_{FE} \quad (88)$$

which is found via Gauss Block elimination of the LO Jacobian

$$\mathbb{J} = \begin{bmatrix} \mathbb{J}_{EE} & \mathbb{J}_{EF} & \mathbb{J}_{ET} \\ \mathbb{J}_{FE} & \mathbb{J}_{FF} & 0 \\ \mathbb{J}_{TE} & 0 & \mathbb{J}_{TT} \end{bmatrix}. \quad (89)$$

The submatrices can be split into two groups, diagonal matrices

$$\mathbb{J}_{EE,ii} = \left(\frac{1}{\Delta t_n} + \sigma_{E_{i,n}} c \right) \quad (90a)$$

$$\mathbb{J}_{ET,ii} = -4\sigma_{P_{i,n}} acT_{i,n,\ell+1}^3 \quad (90b)$$

$$\mathbb{J}_{TT,ii} = \left(\frac{\rho_i c_{v,i}}{\Delta t_n} + 4\sigma_{P_{i,n}} acT_{i,n,\ell+1}^3 \right) \quad (90c)$$

$$\mathbb{J}_{TE,ii} = -\sigma_{E_{i,n}} c \quad (90d)$$

$$\mathbb{J}_{FF,ii} = \frac{1}{c\Delta t_n} + \sigma_{R_{j,n}} \quad (90e)$$

and matrices with off-diagonal parts

$$\mathbb{J}_{EF,ij} = \hat{\mathbf{n}}_{ij} \cdot \hat{\mathbf{n}}_j \frac{A_j}{V_i} \quad (90f)$$

$$\mathbb{J}_{FE,ji} = c\hat{\mathbf{n}}_j \cdot \left(\frac{\hat{\mathbf{n}}_{ij}}{3\Delta x_j} + \gamma_{ij,n} \right). \quad (90g)$$

The boundary Jacobian is (also with off-diagonal parts)

$$\mathbb{J}_{FE,ji}^{\text{bc}} = -(1 - \alpha_j) \kappa_{j,t}^{\text{out}}. \quad (90h)$$

A.2. Particle corner case

Special caution is necessary if a particle leaves a cell at a corner. This is indicated by two surfaces with the same distance. Even though this case seems unlikely, it has been observed during calculations. If a particle crosses a cell corner, the next cell it enters is ambiguous. If not handled correctly, the particle can enter a cell without actually being within the cell boundaries. Our mitigation strategy is to move the intersection into one of the connected surfaces, resolving all ambiguity. Due to floating-point round-off issues, this is triggered if the particle crosses a surface in a small circle around a corner, with a fraction of the distance from the surface to the cell center as radius. Our solution addresses round-off issues and is valid for all mesh sizes.

A.3. Negative temperatures

A linear source representation can lead to negative values. To prevent this we check all corners of a cell, and adjust, if necessary the slope. For all vertices v of cell i , perform the test

$$\bar{\Theta}_{i,n} + \tilde{\Theta}_{i,n} \cdot (\mathbf{x}_v - \mathbf{x}_{C,i}) < \Theta_{\min} \quad (91)$$

where Θ_{\min} is the lowest allowed temperature. If the inequality is true, we will adjust the slope such that the value at the vertex is Θ_{\min} . For this, we use the equation

$$\bar{\Theta}_{i,n} + \beta_v \tilde{\Theta}_{i,n} \cdot (\mathbf{x}_v - \mathbf{x}_{C,i}) = \Theta_{\min} \quad (92)$$

and solve for

$$\beta_v = \frac{\Theta_{\min} - \bar{\Theta}_{i,n}}{\tilde{\Theta}_{i,n} \cdot (\mathbf{x}_v - \mathbf{x}_{C,i})}. \quad (93)$$

The slope is corrected as

$$\tilde{\Theta}'_{i,n} = \beta_v \tilde{\Theta}_{i,n} \quad (94)$$

This will reduce the slope so that all corners with the negative values are reset to the minimum temperature or above, while preserving the cell average.